AIMS Materials Science, 5(5): 957–999.
DOI: 10.3934/matersci.2018.5.957
Received: 13 August 2018
Accepted: 10 October 2018
Published: 24 October 2018

http://www.aimspress.com/journal/Materials

Review

Novel nanostructured materials by atomic and molecular layer deposition

Jiyu Cai, Qian Sun and Xiangbo Meng*

Department of Mechanical Engineering, University of Arkansas, Fayetteville, AR 72701, the United States

*** Correspondence:** Email: xbmeng@uark.edu; Tel: +14795754912; Fax: +14795756982.

Abstract: Nanostructured materials (NMs) are the materials with a microscopic structure of 1–100 nanometers. NMs can outperform their bulk counterparts, due to their reduced sizes. In terms of dimensionality, NMs can be classified into zero-dimension (0D), 1D, 2D, and 3D. Atomic and molecular layer deposition (i.e., ALD and MLD) are two unique techniques for fabricating and designing novel NMs, featuring their unique capabilities for material growth with excellent uniformity, unrivaled conformal coverage, and precise controllability at low temperature. As a result, a large variety of NMs by ALD and MLD have found applications in a wide range of areas. In this work, we focus on summarizing the strategies of ALD and MLD for various NMs and exemplify their applications in surface engineering and new energies.

Keywords: nanostructured materials; atomic layer deposition; molecular layer deposition; surface engineering; catalysis; rechargeable batteries

1. Introduction

Nanostructured materials (NMs), typically one of their physical dimensions in the range of 1–100 nm [1–3], have been attracting many interests due to their exceptional properties over traditional bulk materials. With material size down to the nanoscale, the percentage of atoms on the surface and the surface-to-volume ratio (or specific surface area) dramatically increase [4,5]. More atoms on the surface may have much more dangling bonds to actively form bonds with adjacent molecules or particles, affecting the intrinsic properties of NMs [4]. For instance, NMs can exhibit many exotic properties, such as increased chemical activity [3], lowered melting point [3], large band

gap [5], fast electrons/ions transportation [6], highly efficient photon absorption [7], and improved mechanical stress and strain [8]. Two general synthesis strategies have been practiced for NMs, i.e., top-down methods (e.g., optical [9,10], E-beam [11–13], nanoimprint [14–16], and scanning probe [17–19] lithography methods) and bottom-up methods (i.e., atomic layer deposition [20–22], solution-based methods [23–25], and vapor phase deposition [26–29]). The bottom-up methods have shown tremendous promises in manipulating atoms and molecules to establish complex nanostructures with dimensions of <10 nm [10], which is difficult to be achieved through the top-down processes [30,31].

The classification of nanostructured materials by dimensionality was first proposed by Fiorani and Sberveglieri in 1994 [32], suggesting zero-dimension (0D), 1D, 2D, and 3D. The classification later has experienced some modifications. Now, 0D NMs are defined as the materials with all three dimensions in nanoscale and no significant difference in size between the longest and shortest axes [33,34], e.g., nanoparticles [35], core-shell quantum dots [36,37], nano-onions [38], and hollow nanospheres [39]. 1D NMs are those that two dimensions are within the nanoscale and one dimension beyond nanoscale [40], e.g., nanowires [41,42], nanorods [43], nanotubes [41], and nanoribbons [42]. 2D NMs are generally considered as materials with a thickness of a few atomic layers and the other two dimensions beyond the nanoscale [33], e.g., nanosheets [44,45], nanoplates [46–48], nanodisks [49] and nanowalls [50–53]. 3D NMs are the materials having all three dimensions beyond nanoscale but exhibiting the merits of nano-size effect [33]. Thus, herein the dimension refers to the morphological characteristics of resultant materials, not their inherent structures.

To date, NMs have explored their applications in a large variety of areas, such as agriculture [54–57], food [58–60], medicine [61–66], environmental science [67], cosmetics [68–72], textiles [73–77], water purification [78–80], and sensor technology [81–84]. In addition, NMs are very important for developing energy harvest devices (e.g., solar cells) and energy storage devices (e.g., lithium-ion batteries). For example, solar cells have applied semiconductive materials of 0D (nanoparticles) [85–90], 1D (nanowires, nanotubes) [91–98], 2D (nanodisks, nanosheets, and multilayered nanofilms) [99–104], and 3D (mesoporous structures) [105–109] nanostructures. Employing nanostructured semiconducting cathodes, the solar cells were found to deliver higher photo-conversion efficiency than bulk semiconducting cathodes [110]. In addition, lithium-ion batteries (LIBs) have been dominating portable electronics since commercialization in 1991 due to their high energy density [111]. However, many practical problems have been plaguing the development of LIBs [112], such as volume expansion of electrode materials, lithium dendritic growth and formation of solid electrolyte interface (SEI). NMs are very effective to resolve these problems via surface protection on electrode, separator modification, and preparation of solid state electrolyte, thus improving the cycling life, electrochemical and mechanical stability of the battery systems [112–115].

Since the very beginning of the 21st century, atomic layer deposition (ALD) has emerged as a new bottom-up process for various nanostructures [116,117]. ALD features its atomic-scale growth controllability [118,119], unrivaled conformal coatings in high-aspect-ratio (HAR) substrates up to 100,000:1 [120], excellent uniformity over large-scale substrates [121,122], and low growth temperature (<400 ℃ and even down to room temperature) [123–125]. As a result, ALD has precisely enabled various nanostructures. To date, ALD has been applied for a large range of inorganic materials, including elements [126], oxides [127–129], nitrides [130–132],

sulfides [133–135], and ternary or even high-level compounds [136–138]. Recently, the fundamentals of ALD and its applications for nanostructures have been discussed in literatures [139,140]. For instance, Marichy et al. [139] in 2012 have summarized the applications of novel NMs by ALD in energy conversion and storage.

Analogous to ALD, molecular layer deposition (MLD) as the sister technique is exclusively for depositing purely organic or hybrid organic–inorganic films. MLD to date has synthesized many different polymeric films, e.g., polyamide [141], polyurea [142], polyurethane [143], polyimide [144,145], and polyazomethine [146]. The organic–inorganic hybrid films via MLD include alucones [147], zincones [148–155], zircones [156,157], titanicones [136,158–160], hafnicones [161], and vanadicones [162]. All these have recently been well documented in the review by Meng [163].

In this review, we provide an overview on the strategies via ALD or/and MLD for different NMs. Following this introductory section, a brief description on both ALD and MLD techniques is provided. NMs via ALD or/and MLD are discussed in the following parts. Then, we highlight the enhancement of several promising applications using NMs fabricated by ALD or/and MLD, including surface engineering, catalysis, and batteries. The last section summarizes the significance of NMs and outlooks the future development of NMs via ALD/MLD.

2. Briefing on ALD/MLD

The ALD technique was emerged in the 1960s in former Soviet Union [164,165] and the 1970s in Finland [20,166]. A typical ALD cycle of binary compounds is composed of two alternative self-limiting gas–solid reactions induced by two exposures of precursors [167–172]. A representative ALD process is the ALD-Al_2O_3 using trimethylaluminum (TMA) and water as precursors. The first step is the introduction of TMA to react with a substrate surface, as described by Eq 1 (see Figure 1a) [163]. Then, a purging step is used to remove excessive TMA and the byproduct CH_4. In a following step, the second precursor of H_2O is dosed and therefore induces another surface reaction, as described by Eq 2. Then, another purging is conducted to evacuate excessive H_2O precursor and the gaseous byproduct CH_4.

$$\text{├OH} + \text{Al(CH}_3\text{)}_3\text{ (g)} \rightarrow \text{├O–Al(CH}_3\text{)}_2 + \text{CH}_4\text{ (g)} \quad (1)$$

$$\text{├O–Al(CH}_3\text{)}_2 + 2\text{H}_2\text{O (g)} \rightarrow \text{├O–Al(OH)}_2 + 2\text{CH}_4\text{ (g)} \quad (2)$$

where "├" refers to the substrate surface and "g" indicates the gaseous phase of precursors or byproducts. Apparently, ALD deposits inorganic thin films in a repeatable layer-by-layer mode, and the film growth is typically influenced by three key parameters: substrate, temperature, and precursor. Different from other source-controlled vapor-phase methods (e.g., chemical and physical vapor deposition), ALD is surface-controlled and this leads to many advantages in film deposition, such as extremely uniformity, unrivaled conformality, and excellent controllability at the atomic level growth.

Similar to ALD, MLD also is a surface-controlled vapor phase process (see Figure 1b). ALD is exclusive for inorganic materials, while MLD features its preciseness for growing purely organic or inorganic–organic hybrid films. A typical MLD process can be exemplified by the deposition of the alucone AlEG, using TMA and ethylene glycol (EG, $HOCH_2CH_2OH$) as precursors [147], as described in Eqs 3 and 4.

$$\text{├OH} + \text{Al(CH}_3\text{)}_3\text{ (g)} \rightarrow \text{├O–Al(CH}_3\text{)}_2 + \text{CH}_4\text{ (g)} \quad (3)$$

$$\text{├O–Al(CH}_3\text{)}_2 + 2\text{HOCH}_2\text{CH}_2\text{OH (g)} \rightarrow \text{├O–Al(OCH}_2\text{CH}_2\text{OH)}_2 + 2\text{CH}_4\text{ (g)} \quad (4)$$

Apparently, the molecular fragment of $–OCH_2CH_2O–$ attached in the MLD-alucone is far much larger than the atomic part of –O– in the ALD-Al_2O_3. This makes the MLD film of the aluminum alkoxide (i.e., AlEG) grow much faster than the analog of the ALD-Al_2O_3. More details about MLD processes and growth characteristics can be found in the recent review by Meng [163].

In spite of these progresses, ALD and MLD are still experiencing their rapid expanding phases, and they are becoming new research thrusts in many applications such as surface engineering, new energies, and catalysis. Along with their widening paces, the costs of ALD and MLD processes are hopefully to reduce in the near future, for they are closely related to the needs and supplies of their precursors. At the current stage, the precursors of ALD and MLD processes in most cases are only needed in small amounts, leading to their high costs.

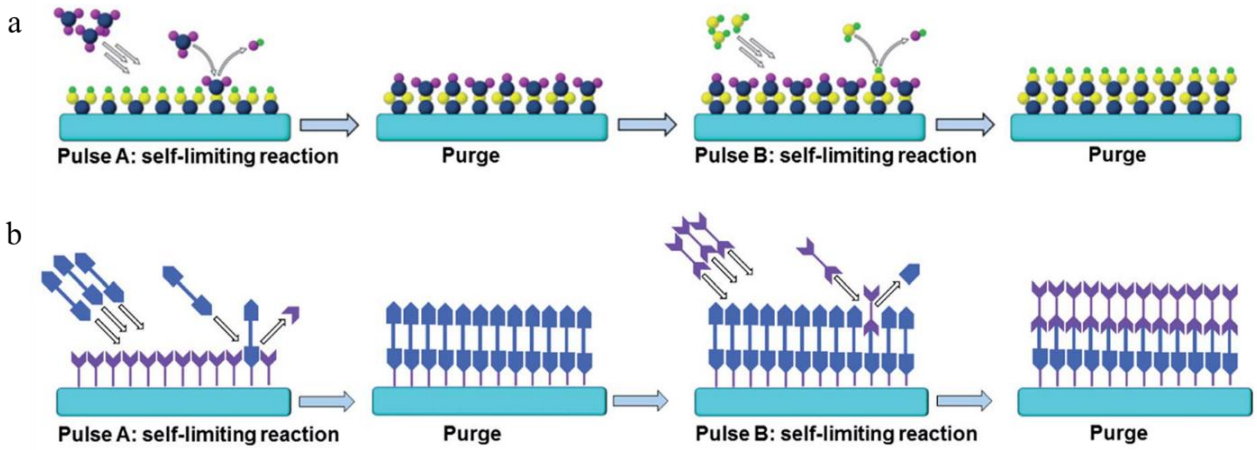

Figure 1. Schematic illustrations of (a) ALD and (b) MLD processes [163]. Reprinted (adapted) with permission from Ref. [163]. Copyright (2017) Royal Society of Chemistry.

3. Nanostructured materials by ALD

3.1. 0D NMs

Due to its surface-controlled nature, ALD exhibits a great promise for fabricating novel 0D nanostructures. The synthesis of copper nanoparticles via ALD was first reported in 2003 by Johansson et al. [173]. In the study, a three-step ALD process was conducted: (i) dosing CuCl, (ii) dosing H_2O to react CuCl with the production of CuO particles, and (iii) dosing H_2 to reduce CuO into Cu particles. SEM images showed that, after 400 cycles of ALD Cu deposition on alumina substrates at 450 ℃, there were well-distributed Cu nanoparticles in average diameter of 60 nm.

ALD also enables to coat a variety of 0D substrates into new 0D nanostructures. ALD was first reported for coating 0D nanoparticles in 2005 by George's group [174], when SnO_2 coatings were deposited on Al and ZrO_2 nanoparticles in the range of 250–1000 ℃. The researchers used $SnCl_4$ and

H_2O_2 as precursors for the SnO_2 deposition. The resultant Al@SnO_2 nanoparticles were then tested for thermite applications, which reacted much more quickly and violently than the uncoated Al particles. Subsequently, there have been an increasing number of studies using ALD to coat various thin films (i.e., Al_2O_3 [175–177], TiO_2 [178], and ZnO [178]) over nanoparticle substrates (i.e., SiO_2 [176,179], ZrO_2 [179], Ag [178], Ni [180], and polyethylene [175]) for 0D core–shell nanostructures. For instance, Hakim et al. [177] coated 5 nm Al_2O_3 over 26 nm ZrO_2 nanoparticles using TMA and H_2O as ALD precursors. Uniform and conformal Al_2O_3 thin films were confirmed by transmission electron microscopy (TEM) and scanning electron microscope (SEM). Similarly, Hakim et al. [176] deposited 5 nm Al_2O_3 on 40 nm SiO_2 nanoparticles using the same ALD procedure (see Figure 2a).

Analogous to the 0D core-shell nanoparticle strategies, the ALD technique has also been used for developing various hollow nanospheres. In 2006, Kei et al. [181] conducted the first effort to form a smooth and conformal ALD Al_2O_3 coating on hydrothermally synthesized polystyrene nanospheres. The Al_2O_3 coating was deposited at 200 ℃ for 200 ALD cycles using TMA and H_2O as precursors. The Al_2O_3 film thickness was confirmed being ~24 nm by X-ray reflectivity (XRR). Through heating the resultant core-shell nanostructures in air, Kei et al. [181] enabled the hollow nanospheres of Al_2O_3. The similar strategy then has been applied for producing other nanospheres. Ras et al. in 2007 [182] deposited a conformal coating of Al_2O_3 at 80 ℃ on another polymer nanospheres of ~40 nm synthesized using polystyrene (PS) and poly-(4vinylpyridine) (P4VP) block copolymers. Then, the polymer cores were thermally decomposed at 300 ℃ in the N_2 atmosphere, yielding hollow Al_2O_3 nanospheres. This work also demonstrated the ALD capability in depositing films over temperature-sensitive polymers. Moreover, TiO_2 and ZnO hollow nanospheres were also reported by Justh et al. [183]. TiO_2 and ZnO coatings were first deposited on hydrothermally synthesized carbon nanospheres (CNSs) using the precursors of $TiCl_4/H_2O$ and DEZ/H_2O at 250 ℃, respectively. Then, the CNS-metal oxide composites were heated to 700 ℃ in ambient environment to remove the CNS cores (see Figure 2b,c).

Furthermore, derived from 0D core-shell strategies, a facile and robust approach for fabricating highly ordered TiO_2 nanobowls via ALD was first demonstrated by Park et al. in 2012 [184]. The fabrication process of the patterned 0D TiO_2 nanobowls includes a series of procedures: (i) the self-assembly of PS nanospheres on glass and polyethylene terephthalate (PET) substrates via a scooping transfer technique (see Step A in Figure 2d), (ii) an ALD-deposited 48-nm thick TiO_2 coating over PS nanospheres at 80 ℃ using the precursors of titanium(IV) iso-propoxide and water (see Step B in Figure 2d), (iii) a CF_4-based reactive ion etching (RIE) process to remove the top of the TiO_2-coated PS nanospheres (see Step C in Figure 2d), and (iv) a annealing process at 450 ℃ for 2 h to remove the PS nanospheres and also transform the amorphous phase of the ALD-deposited TiO_2 to the crystalline anatase phase (see Step D in Figure 2d). The top- and side-view SEM images displayed the eventual 2D TiO_2 nanobowls (see Figure 2e), respectively. The TiO_2 nanobowl structures could be scaled up to various substrates for the potential applications in optical, electronic, and biological devices.

To date, there has been a large number of papers documented in literature for 0D nanostructures via ALD processes. ALD coatings are very feasible in tuning the surface properties of the original nanoparticles, such as serving as protective coatings to prevent particles from oxidation [185], reducing electrical conduction [186], and improving optical [187] or mechanical [188] properties of particles. All these are due to the ALD's unique growth mechanism and growth characteristics, i.e.,

the surface-controlled deposition with the atomic-level growth of high-quality films at low temperatures. Recently, the ALD technique has also been reported to integrate with the traditional fluidized-bed technology for massive production of 0D nanostructured materials [189]. This has laid a venue to expand ALD into more applications.

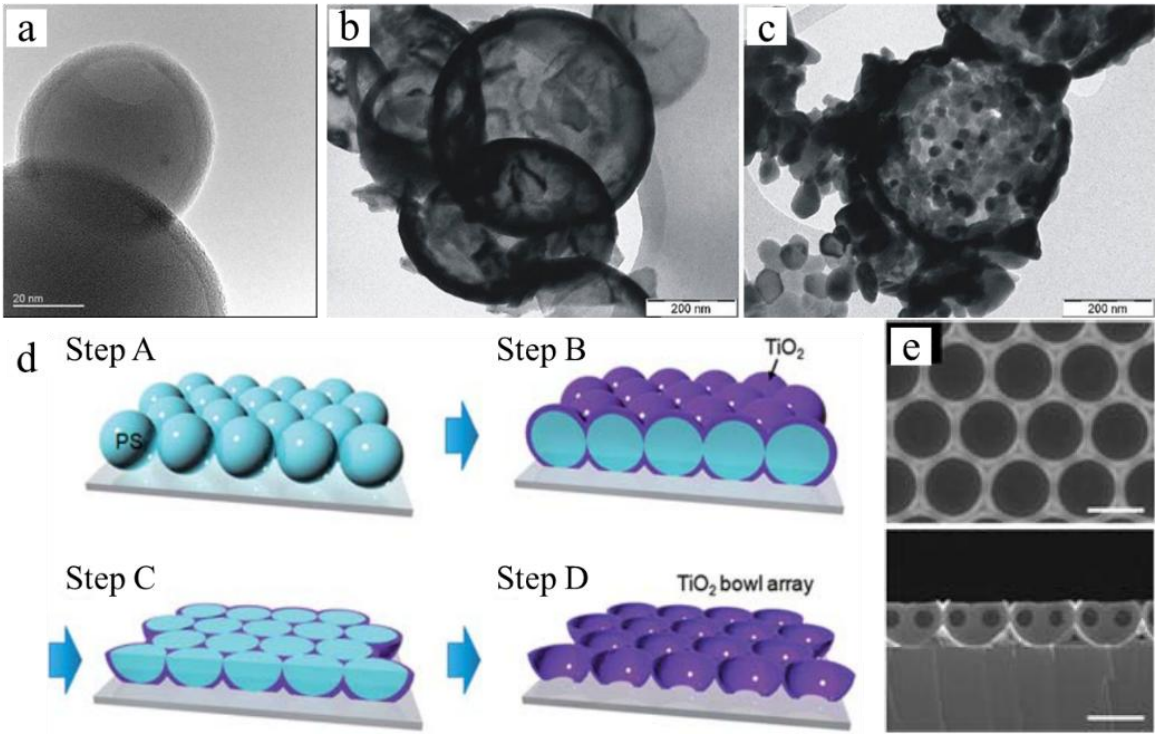

Figure 2. (a) TEM images of silica nanoparticles with 50-cycle Al_2O_3 coating [176]. Reprinted (adapted) with permission from Ref. [176]. Copyright (2005) John Wiley and Sons; TEM images of (b) TiO_2 and (c) ZnO hollow nanospheres after the removal of carbon nanospheres at 700 ℃ in the ambient [183]. Reprinted (adapted) with open access permission under a CC BY license (Creative Commons Attribution 4.0 International License) from Ref. [183]. Copyright (2005) Scientific Reports; (d) Schematic diagram of the fabrication process of the patterned 2D TiO_2 nanobowl structure: (Step A) a self-assembled monolayer of PS nanospheres on the substrate, (Step B) conformal coating of a TiO_2 layer on a PS nanosphere monolayer-assisted substrate by ALD, (Step C) PS@TiO_2 hemispheres created by the CF_4-based RIE process, and (Step D) a TiO_2 nanobowl array fabricated by annealing (450 ℃, 2 h). (e) Top- and side-view SEM images of 0D TiO_2 nanobowl array [184]. Reprinted (adapted) with permission from Ref. [184]. Copyright (2013) Royal Society of Chemistry.

3.2. 1D NMs

There are many different 1D nanostructures, such as nanowires, nanotubes, nanorods, nanobelts, and so on. In 2002 Solanki et al. [190] reported an ALD process for 1D ZnSe/CdSe superlattice growth. The researchers first pretreated a silicon wafer covered with a 100 nm SiO_2 layer using a

0.1% solution of poly-L-lysine for 1 min, and then coated a layer of ~6 nm Au nanoparticles using gold-nanocluster solution. The coating of Au nanoparticles was examined for adhesion using atomic layer microscope (AFM). A ZnSe/CdSe composite was deposited on the substrate at the temperatures of 400 to 420 ℃, followed by a sequence of 10 ZnSe monolayers and 5 CdSe monolayers. The precursors for ZnSe and CdSe were Zn/Se and Cd/Se, respectively. As a result, a 5 nm thick nanowire was grown (see Figure 3a). High-resolution TEM (HRTEM) analysis confirmed the excellent crystallinity of ZnSe and CdSe (see Figure 3b). This composite nanowire had a photoluminescence effect to excite the 450 and 540 nm wavelength photons.

In addition to the synthesis of 1D nanowires, ALD has also enabled 1D core-shell nanotubular structures. In 2003, Min et al. [191] deposited a ~6 nm Ru thin film on carbon nanotubes (CNTs) using $Ru(od)_3$/n-butylacetate solution and O_2 as ALD precursors at 300 ℃. The resultant CNT@Ru core-shell composite was then oxidized at 500 ℃ with the removal of the inner CNTs, resulting in pure RuO_2 nanotubes. HRTEM confirmed that Ru films grew uniformly and conformally over the inner and outer surfaces of CNTs (see Figure 3c,d). Based on CNTs, there have been a large amount of 1D nanotubular structures reported in literature, such as ntrigen-doped CNTs (NCNTs)@ZrO_2 (see Figure 3e) [192], NCNTs@$Li_4Ti_5O_{12}$ [193], NCNTs@SnO_2 [194], TiO_2 nanotubes [195], single-walled CNTs@Cu_2S [196], single-walled CNTs@GaS [197], and CNT@Fe_2O_3 [198].

Besides CNTs, another popular ALD strategy for nanotubes is based on the use of anodic aluminum oxide (AAO) templates. Typically, AAO templates can be prepared by a two-step anodization procedure [199]. First, aluminum sheets were electropolished in a solution of perchloric acid and ethanol, and then anodized in an oxalic acid. Second, the unreacted Al was selectively etched away in a saturated $HgCl_2$ solution and immersed in a phosphoric acid to etch the barrier layer. Elam et al. in 2006 [199] deposited various ALD conformal coatings (including Al_2O_3, TiO_2, V_2O_5, ZnO, and Pd) into nanopores of porous AAO templates. SEM images presented the top view of 15 nm ALD Al_2O_3 coated AAO template (see Figure 3f), showing conformal Al_2O_3 coating grown along high aspect-ratio AAO nanotubular structure. Through further etching AAO templates away using a base solution (e.g., KOH and NaOH), the inner deposited ALD layers could be remained in nanotubular structures, e.g., SnO_2 [200] and TiO_2 [195] nanotubes. For instance, Meng et al. [200] demonstrated a synthesis strategy towards highly structure-tunable SnO_2 nanotube arrays of high aspect ratio (up to 300:1) using ALD. The fabrication procedures of the patterned 1D SnO_2 nanotubes are as follows: (i) ALD SnO_2 deposition on the inner surfaces of nanopores of AAO templates using $SnCl_4$ and H_2O, resulting in the formation of tubular SnO_2 nanostructures (see A and B in Figure 3g), (ii) the removal of the top covering of AAO by mechanically polishing to expose an array of SnO_2 nanotubes (see C in Figure 3g), and (iii) a wet-etching of NaOH to dissolve AAO and then harvest an array of separated SnO_2 nanotubes (see D in Figure 3g). Not limited to above cases, there have many more studies using ALD for 1D NMs [201–208]. All these 1D NMs have taken advantages of ALD's surface-controlled film growth.

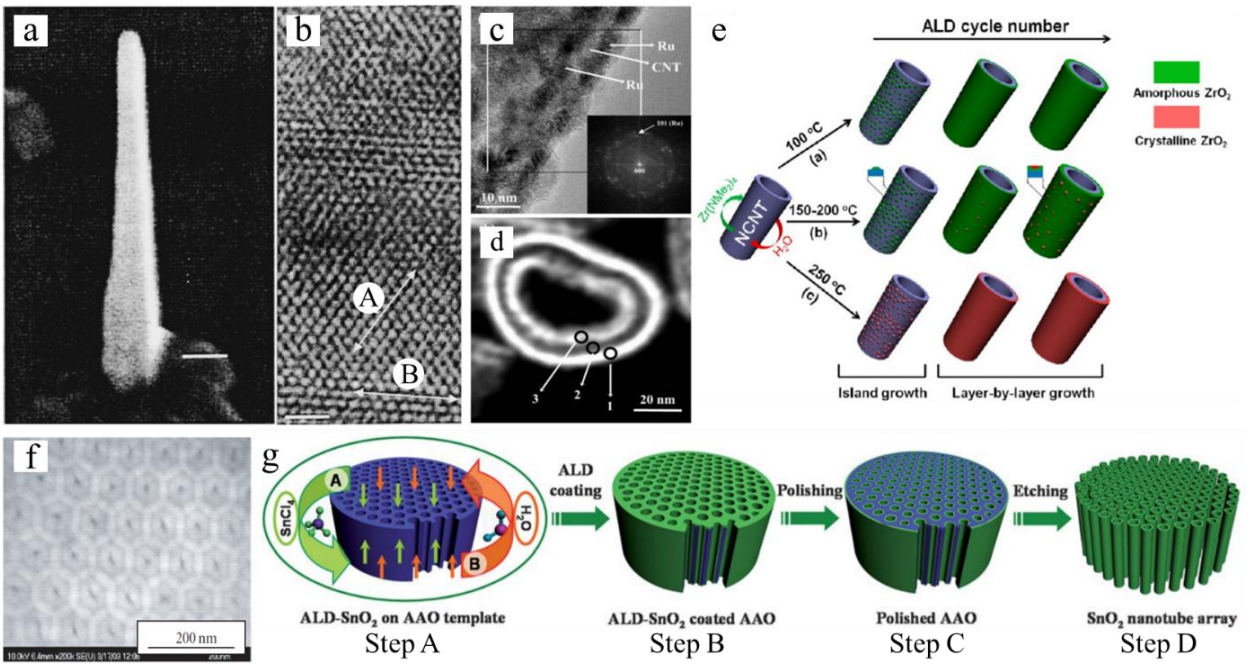

Figure 3. (a) SEM images of a ZnSe/CdSe nanowire and (b) HRTEM images of ZnSe/CdSe superlattice showing (111) plane of ZnSe for direction A and (111) plane of CdSe for direction B [190]. Reproduced from [190] with the permission of AIP Publishing; (c) HRTEM image and (d) Z-contrast image of a Ru-coated CNT nanotubes, denoting the conformal coating on inner and outer surface of CNT [191]. Reprinted (adapted) with permission from Ref. [191]. Copyright (2003) John Wiley and Sons; (e) Schematic diagram for the growth mechanism of ALD-ZrO_2 on NCNTs at (a) 100 ℃, (b) 150–200 ℃, and (c) 250 ℃ [192]. Reprinted (adapted) with permission from [192]. Copyright (2012) American Chemical Society. (f) Top view SEM images of AAO template after 15 nm ALD Al_2O_3 coating, showing high conformity [199]. Reprinted (adapted) with permission from Ref. [199]. Copyright (2011) Cambridge University Press; (g) Schematic fabrication of SnO_2 nanotubes via template-directed ALD: (Step A) the ALD-SnO_2 coating on an AAO template, (Step B) the ALD-coated AAO template, (Step C) the mechanically polished AAO template, and (Step D) the received SnO_2 nanotube array [200]. Reprinted (adapted) with permission from Ref. [200]. Copyright (2011) Royal Society of Chemistry.

3.3. 2D NMs

ALD was first performed for 2D nanofilms, and thus 2D nanofilms are the most common format of different nanostructures. Among the 2D nanofilms, ALD particularly enables nanolaminates consisting of multi-layered materials. Each layer in nanolaminates can be precisely controlled with atomic-scale thickness. This is very convenient for developing new functional materials with tunable composition and properties. In this regard, KuKli in 1997 [209] reported 2D Al_2O_3/Ta_2O_5 and ZrO_2/Ta_2O_5 nanolaminates (see Figure 4a), achieving low-leakage and high-permittivity dielectric properties. Elam et al. [210] later fabricated ZnO/Al_2O_3 nanolaminates in 2002

using TMA/H_2O for amorphous Al_2O_3 and DEZ/H_2O for crystalline ZnO. It was found that the Al_2O_3 layer could suppress the crystal growth of ZnO films and thus the surface roughness of the ZnO/Al_2O_3 nanolaminates could be tuned.

Subsequently, there have been many more studies invested for various nanolaminates, such as HfO_2/Ta_2O_5 [211], Al_2O_3/TiO_2 [211], AlP/GaP [212], HfO_2/SiO_2 [213], and Y_2O_3/ZrO_2 [214]. These nanolaminates feature their tunable physical properties [211,212,214–216]. For instance, Zaitsu et al. employed ALD Al_2O_3/TiO_2 nanolaminates for tunable optical refractive index over a wide range from 1.870 to 2.318 [215]. The researchers also interpreted that film thickness of the alternating Al_2O_3/TiO_2 layers were related to both the number of each sublayer cycle and the certain growth rate of each material (see Figure 4b). Therefore, the volume concentration of the Al_2O_3 coating could be manipulated by adjusting the cycling number of the Al_2O_3 sublayer in the binary ALD system. Ginestra et al. in 2007 [214] reported a solid-state electrolyte membrane of Y_2O_3/ZrO_2. The as-deposited nanolaminates were post-annealed for crystallization at 950 °C for 2 hours, allowing inter-diffusion between nanolaminate films. A comparison between the as-deposited and annealed samples in the cross-sectional HRTEM images (see Figure 4c,d) showed the inter-diffusion. The annealed films, consisting of the diffused crystal ZrO_2 and Y_2O_3 composite, were investigated for their electrical conductivity. They found that the nanolaminate having 2 mol% Y_2O_3 enabled a conductivity 15 times higher than that of the nanolaminate having 3 mol%. This clearly showed that ALD is a very precise tool for optimizing materials' properties.

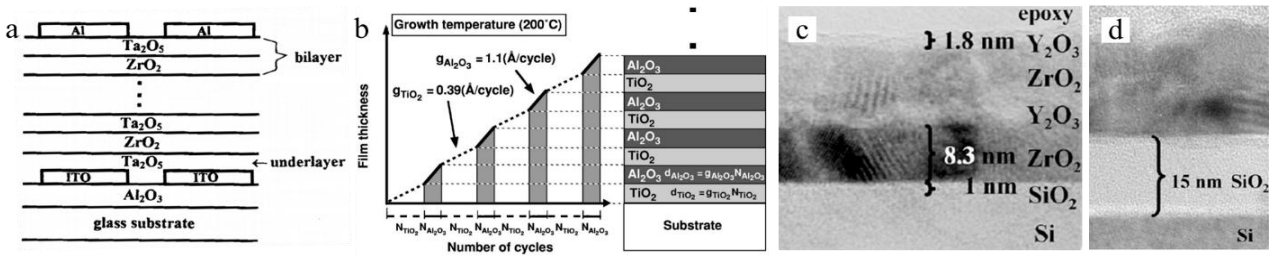

Figure 4. (a) A schematic representation of the nanolaminate structure of alternative ZrO_2 and Ta_2O_5 films [209]. Reprinted (adapted) with permission from Ref. [209]. Copyright (1997) The Electrochemical Society; (b) A schematic explanation of the alternately deposited nanoscale sublayers and the relationship between layer thickness (dAl_2O_3 and $dTiO_2$) and the number of growth cycles (NAl_2O_3 and $NTiO_2$) [215]. Reprinted (adapted) with permission from Ref. [215]. Copyright (2002) The Electrochemical Society; Cross-sectional HRTEM images of (c) as-grown Y_2O_3/ZrO_2 nanolaminate showing clear layer interfaces and (d) the interdiffused Y_2O_3/ZrO_2 nanolaminate after annealing [214]. Reprinted (adapted) with permission from Ref. [214]. Copyright (2007) The Electrochemical Society.

3.4. 3D NMs

Owing to its conformal coating capability, ALD can also be used for developing 3D novel nanostructures based on complex substrates. Using SiO_2 inverse opal photonic crystals as substrates, for instance, Graugnard et al. in 2006 [217] fabricated 3D TiO_2 inverse-shell opals. The fabrication process can be divided into following procedures: (i) preparation of opal structure using self-assembled and sintered silica nanospheres of ~450 nm (see A in Figure 5a), (ii) infiltration of a template with ZnS or Al_2O_3 sacrificial layer (see B in Figure 5a) and TiO_2 dielectric material (see C in Figure 5a) in silica opal structure via ALD, (iii) inversion of the opal structure by removing both the original template (see D in Figure 5a) and the sacrificial layer (see E in Figure 5a), and (iv) reinfiltration (or backfilling) of the new template with additional dielectric material (see F in Figure 5a). SEM images exhibited the cross section of a doubly infiltrated silica opal template by 15 nm ZnS and 20 nm TiO_2 layers (see in Figure 5b), a thin backbone of TiO_2 after the removal of the silica nanospheres and sacrificial ZnS layer (see in Figure 5c), and backfilling with an additional 20 nm TiO_2 layer on inverse opal structure (see in Figure 5d). The 3D TiO_2 opal structure greatly enhanced photonic properties with a 58% increase of reflective index. Similarily, King et al. [218] demonstrated 3D TiO_2/ZnS:Mn/TiO_2 inverse opal structures via ALD. The resultant 3D structure enabled the combination of the strong photoluminescent properties of ZnS:Mn with the full refractive index of TiO_2. These papers successfully demonstrated the unrivaled conformality and atomic-scale growth from the vapor-phase ALD technique.

Another representative 3D nanostructure, gyroid-structured 3D ZnO networks via ALD, was demonstrated by Kim et al. in 2014 [219]. They first replicated periodic 3D gyroid networks generated by the self-assembly of polystyrene (PS) in solution-based method. Then, conformal ZnO coating was deposited via ALD on the 3D networks at 80 ℃ using DEZ and H_2O as precursors. The post-process of O_2-plasma treatment at 400 ℃ was conducted for 10 min to remove the PS template, followed by the annealing process at 450 ℃ to transform ZnO to higher crystallinity. Compared with as-synthesized PS networks, the annealed ZnO interconnected skeletons remained 3D gyroid networks with an average pore width of 30 nm (see Figure 5e). Kim et al. [219] revealed that the conformal 3D ZnO networks resulted from the ALD principle of surface-limited reactions, promising for photovoltaic devices.

Moreover, 3D graphene nanosheets (GNS) modified by ALD thin films have been successfully demonstrated, such as SnO_2-GNS [220], TiO_2-GNS [128], and ZrO_2-GNS [221] composites. Liu et al. in 2013 [221] deposited ZrO_2 films on wrinkled GNS via ALD using $Zr(NMe_2)_4$ and H_2O. The pristine GNS with wrinkle thickness of ~4 nm (see Figure 5f) was derived from thermal reduction of graphite oxide (GO). SEM image showed the conformal and uniform ZrO_2 films with the wrinkle thickness of ~19 nm grown on GNS wrinkles at 250 ℃ (see Figure 5g). This work demonstrated the excellent conformity and uniformity of ALD thin film over the wrinkled graphene sheets with extremely high surface ratio.

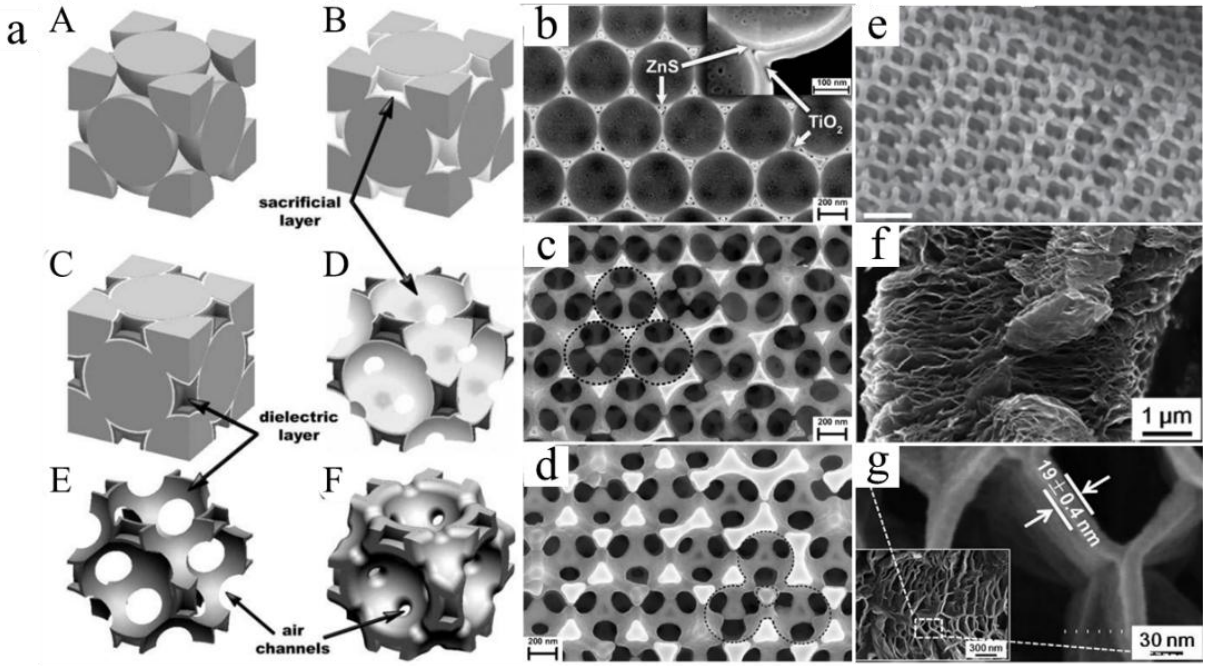

Figure 5. (a) Schematic representation of preparation procedures of the inverse opal structure: the original opal template in (A) infiltrated with a conformal sacrificial film via ALD, resulting in the new template shown in (B); infiltration of dielectric film in the remaining air volume (C); (D) the removal of the original template creating close-packed interconnected dielectric matrix with sacrificial layer; (E) the removal of the sacrificial layer; (F) backfilling with additional dielectric layer. SEM images of cross sections of inverse-opal fabrication: (b) two-layer infiltrated 450 nm SiO_2 opal with a 15 nm sacrificial ZnS layer and 20 nm TiO_2 infiltration, (c) the inverse structure of a TiO_2 backbone by removing SiO_2 spheres and ZnS layer, and (d) backfilling with additional 20 nm of TiO_2 for inverse opal [217]. Reprinted (adapted) with permission from Ref. [217]. Copyright (2006) Advanced Functional Materials. (e) Side-view SEM images at a 45 ° angle of ALD ZnO-coated gyroid template [219]. Reprinted (adapted) with permission from Ref. [219]. Copyright (2014) Advanced Functional Materials. Comparison of SEM images of (f) the pristine nitrogen-doped graphene sheet (NGS) and (g) 100-cycle ZrO_2–GNS nanocomposites prepared at 250 ℃ [221]. Reprinted (adapted) with permission from Ref. [221]. Copyright (2013) Carbon.

4. Nanostructured materials by MLD and both MLD/ALD

4.1. 0D NMs

MLD exhibits excellent capabilities of conformally and uniformly coating various 0D substrates to prepare novel 0D nanostructures, owing to its surface saturation growth and precise control at the molecular level. Liang et al in 2009 [222] deposited alucone films on silica nanoparticles (250 nm) at 100 ℃ using TMA and EG as precursors in a fluidized bed reactor. Then, the as-prepared samples were soaked in water or oxidized in air to become the porous Al_2O_3 films (see Figure 6a). Yang et al.

in 2013 [223] deposited organic polyimide films on Au nanoparticles using ethylenediamine (EDA) and 1,2,4,5-benzenetetracarboxylic anhydride (PMDA) as precursors, followed by a calcination at 600 ℃ to receive ~2 nm carbon shell on Au (see Figure 6b). These works indicated the capability of MLD preparing inorganic–organic and organic films over nanoparticles, and these films will lead to carbon coating after thermal treatment. Subsequently, MLD has been employed to deposit various ultrathin films (i.e., alucone [222,224–226], titanicone [227], and polyimide [223,228]) over nanoparticle substrates (i.e., silica [222,225,226], SiO_2 [224], TiO_2 [227], titania [226], Au [223] and Zr [228]) for 0D core-shell nanostructures.

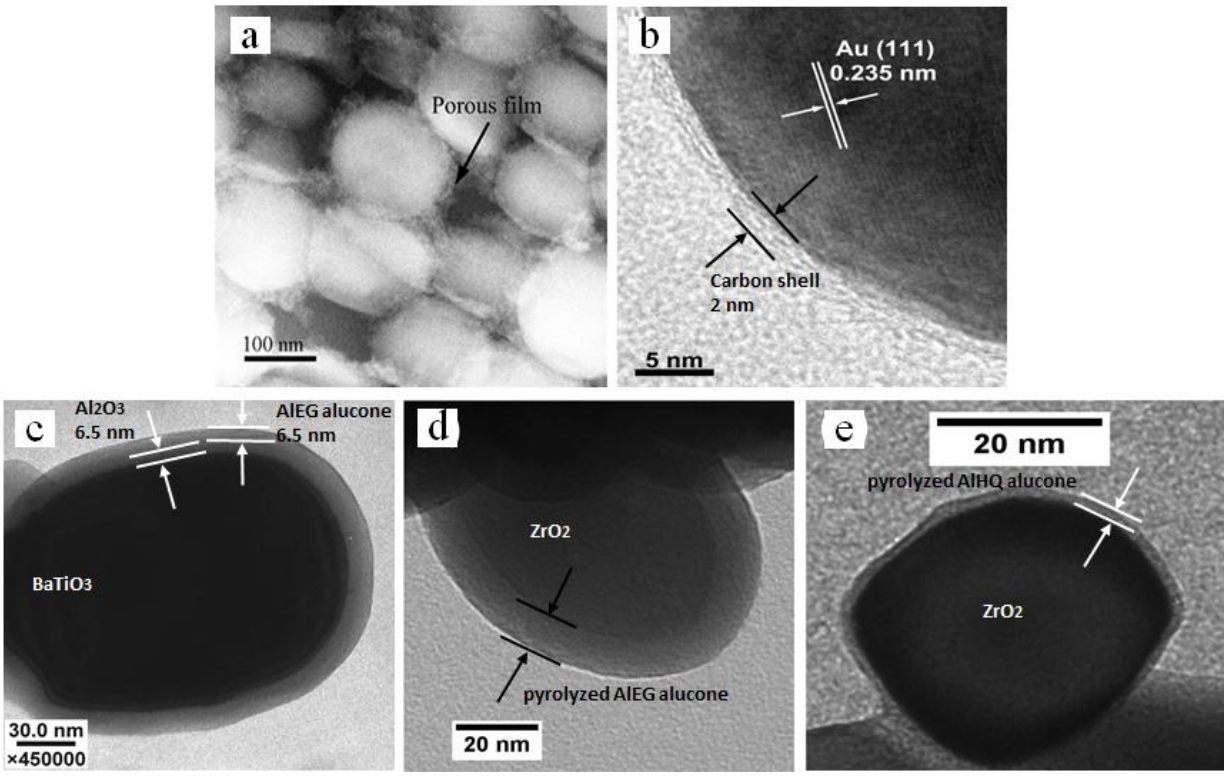

Figure 6. (a) Scanning transmission electron microscopy (STEM) images of 50 cycles of alucone MLD coated 250 nm SiO_2 particles after being soaked in water for 1 day [222]. Reprinted (adapted) with permission from Ref. [222]. Copyright (2009) Royal Society of Chemistry; (b) HRTEM images of Au/C nanoparticles using MLD process [223]. Reprinted (adapted) with open access permission from Ref. [223]. Copyright (2013) Materials; (c) TEM image of a $BaTiO_3$ particle that was sequentially coated at 135 ℃ with 40 cycles of ALD Al_2O_3 and 50 cycles of MLD alucone. The Al_2O_3 and alucone films result in a bilayer film thickness of ~13 nm [147]. Reprinted (adapted) with permission from Ref. [147]. Copyright (2008) American Chemical Society; TEM images of (d) AlEG alucone film on ZrO_2 nanoparticle after pyrolyzed to 850 ℃ and (e) AlHQ alucone film after pyrolyzed to 750 ℃ [229]. Reprinted (adapted) with permission from Ref. [229]. Copyright (2015) American Chemical Society.

The combined ALD/MLD method was also confirmed in preparing 0D nanomaterials. Dameron et al. in 2008 [147] deposited a double layer of Al_2O_3-aluone film on ZrO_2 nanoparticles of <30 nm

and $BaTiO_3$ nanoparticles of <200 nm (see Figure 6c). Al_2O_3 was first deposited by ALD using precursors of TMA and H_2O. Subsequently, alucone was deposited by MLD in the range of 85–175 ℃ using TMA and EG as precursors. DuMont et al. [229] deposited alucone films on ZrO_2 nanoparticles. In this study, three procedures were conducted: (i) depositing ALD Al_2O_3 on the nanoparticles, (ii) depositing alucone films (AlEG or AlHQ) at 150 ℃, and (iii) post-treating the samples at 400–750 ℃ to transform alucone films to Al_2O_3 and carbon composites. TEM image demonstrated that the pyrolysis of AlEG (see Figure 6d) and AlHQ (see Figure 6e) films led to very conformal Al_2O_3/carbon composite films.

4.2. 1D NMs

MLD was employed to deposit organic films (i.e., zincone [149], alucone [230–233], polyurea [234] and polyimide [223]) on different 1D NMs (i.e, Al_2O_3 microtubes [149], CNTs [223,234], polymer fibers [232,233] and nanowires [230,231]) for developing novel 1D nanostructures. For examples, Qing et al. in 2009 [149] deposited zincone films on Al_2O_3 microtubes by MLD using DEZ and EG as precursors. The microtubes were initially prepared by depositing 500 ALD cycles of Al_2O_3 onto polyvinyl alcohol fibers (PVA), followed by thermal treatment at 400 ℃ to remove PVA. TEM exhibited the comparison of original Al_2O_3 microtubes and zincone films of ~20 nm on the inside and outside of microtubes (see Figure 7a). Subsequently, Yang et al. [223] synthesized carbonaceous nanotubes using MLD, following by a series of procedures: (i) depositing polyimide films on AAO templates by MLD using EDA and PMDA as precursors, (ii) thermally treating at 600 ℃ to decompose the polyimide films under protecting H_2/Ar gas into carbonaceous films inside of AAO tubes, (iii) etching AAO template in NaOH solution to obtain carbonaceous nanotubes. Chen et al. in 2015 [234] employed MLD to deposit 11.6 nm polyurea (PU) on MWCNTs using precursors of 1,4-phenylene diisocyanate (PDIC) and ethylenediamine (ED).

In addition, Gong et al. in 2011 [233] deposited alucone films on electro-spun polyvinyl alcohol fiber mats using TMA and GLY as precursors, followed by a thermal treatment to produce hollow Al_2O_3/carbon composite microtubes. This work demonstrated that MLD enabled alucone films with precise control over film thickness, favorable for artificial solid electrolyte interphase (SEI) in lithium-ion batteries.

Nanowires such as CuO [231] and silicon nanowires [230] were used for fabricating novel 1D nanostructures. Qin et al. in 2011 [231] deposited alucone (AlEG) films of ~37 nm on CuO nanowires by MLD using TMA and ethylene glycol (EG) as precursors (see Figure 7b). The resultant alucone/CuO nanowires were transformed to Cu nanoparticles embedded in porous Al_2O_3 nanotubes in H_2 gas at 650 ℃ (see Figure 7c). To clarify, CuO nanowires were chemically reduced into Cu nanoparticles. In addition, the ethyl groups in alucone films thermally decomposed in H_2 gas, resulting in porous Al_2O_3 nanotubes. Following by a calcination at 400 ℃, Cu nanoparticles diffused through porous Al_2O_3 nanotubes to its exterior surface, initially oxidized into Cu_2O and further to CuO (see Figure 7d). Subsequently, Luo et al. in 2015 [230] deposited MLD alucone films of ~5.6 nm on silicon nanowires (SiNWs) (see Figure 7e), in comparison with ALD Al_2O_3 films of ~5.3 nm on SiNWs (see Figure 7f). The alucone coating resulted in a "V-shaped" lithiation shape of the SiNWs (see Figure 7g), resulted from the high Li permeability of the alucone layer. In contrast, the Al_2O_3 coated SiNWs exhibited an "H-shaped" lithiation shape (see Figure 7h) because of the low intrinsic Li^+ conductivity of the Al_2O_3 layer. The researchers demonstrated that MLD was capable of

structurally and chemically modifying the surface of SiNWs to improve the performance of Si nanostructured anodes.

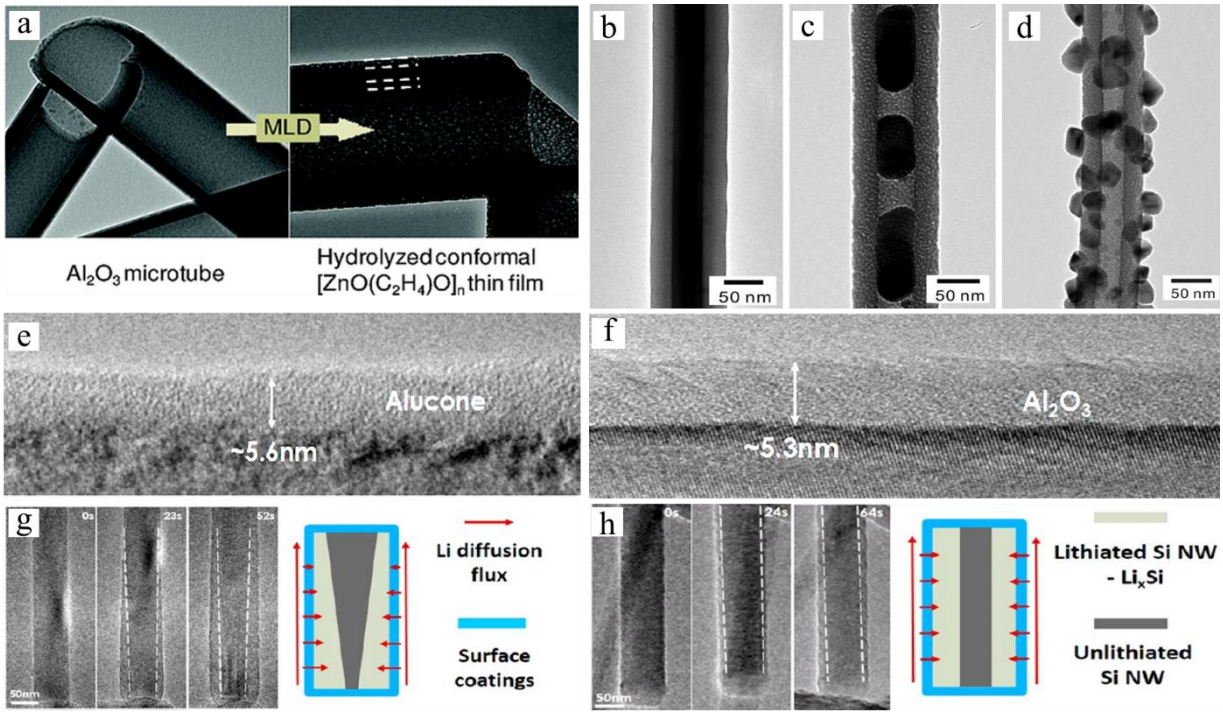

Figure 7. (a) TEM images of Al_2O_3 microtubes and a hydrolyzed Zn-hybrid film deposited on Al_2O_3 microtubes. The white lines indicate the outline of the Zn-hybrid/Al_2O_3/Zn-hybrid laminate [149]. Reprinted (adapted) with permission from Ref. [149]. Copyright (2009) American Chemical Society; TEM images of (b) CuO nanowires coated with a 37 nm thick alucone layer, (c) Cu nanoparticles embedded in porous Al_2O_3 nanotubes (25 nm thick) obtained by reduction in H_2 at 650 ℃, and (d) copper oxide nanoparticles appearing on exterior surface of porous Al_2O_3 nanotubes produced during annealing at 400 ℃ in air [231]. Reprinted (adapted) with permission from Ref. [231]. Copyright (2011) American Chemical Society; Bright-field TEM images of conformal coatings of (e) alucone and (f) Al_2O_3 films on Si nanowires. Time-resolved TEM images show the morphology of lithiation on (g) alucone and (h) Al_2O_3 coated SiNWs, and the schematic illustrations of the Li diffusion paths through the SiNWs that indicates the different lithiation behaviors [230]. Reprinted (adapted) with permission from Ref. [230]. Copyright (2015) American Chemical Society.

4.3. 2D NMs

MLD also was used to fabricate 2D nanostructures. For example, Abdulagatov et al. in 2013 [227] deposited two kinds of MLD titanicone films (TiGL and TiEG) on Si wafers. The resultant samples were pyrolyzed under argon to transform titanicone into TiO_2/carbon composite (see Figure 8a). Lushington et al. in 2015 [235] used the alternated exposures of TMA, EG, and terephthaloyl chloride (TC) by MLD to grow the aluminum alkoxide films. Prior to the MLD process,

a 10 nm ALD Al_2O_3 seed layer was deposited on the polished Si (100) substrate and SiO_2 glass substrate. These hybrid films were then thermally treated at 600–900 ℃ in H_2/Ar to transform the alucone films into Al_2O_3/graphitic–carbon composites. The researchers also addressed that MLD was an effective method to tune the composition of the hybrid films by changing the amount of carbon.

In addition to MLD method, the combined ALD/MLD was also reported in preparing novel 2D nanomaterials [236,237]. Lee et al. [237] applied combined ALD/MLD to prepare ZrO_2-based organic–inorganic nanohybrid thin films for application in organic thin film transistors. First, ZrO_2 was deposited on oxidized Si (100) substrates by ALD at 170 ℃ using $Zr(OC(CH_3)_3)_4$ (ZTB) and H_2O as precursors. Then, alkene-terminated self-assembled organic layers (SAOLs) were prepared by MLD using a repetition of three precursors of $CH_2CH(CH_2)_6SiCl_3$ (7-OTS), ozone, and ZTB. Subsequently, Nisula et al. [236] prepared a thin-film Li_2Q–Li_2TP cell (Pt/Li_2TP/LiPON/Li_2Q/Cu) via ALD/MLD. First, they deposited 500 ALD cycles (~23 nm) of Pt as current collector on 300 mm Si wafers using (methylcyclopentadienyl)trimethylplatinum and oxygen as precursors. Then, the Li_2Q electrode layer (see Figure 8b) was deposited on Pt at 160 ℃ by MLD using lithium bis-(trimethylsilyl)amide (LiHMDS) and hydroquinone (HQ) as precursors. On the Li_2Q layer, the LiPON layer of ~30 nm as solid-state electrolyte was deposited by MLD at 300 ℃ using precursors of LiHMDS and diethyl phosphoramidate (DEPA). Finally, the Li_2TP electrode layer was deposited by 70 MLD cycles at 200 ℃ using LiHMDS and terephthalic acid (benzene-1,4-dicarboxylic acid or TPA) as precursors. At 5 mA/cm^2, the Li_2Q–Li_2TP cell using 15 nm Li_2Q layer could reach 50% of the full capacity within 0.25 s. In addition, this combined ALD/MLD method was utilized to prepare the thin-film Li_2Q/LiPON/Cu cell (see Figure 8c). This study indicated that ALD/MLD thin film techniques enabled the development of advanced thin film electrodes for solid state lithium ion batteries, due to its precise control over thickness and film quality.

Moreover, many studies were devoted to fabricating 2D nanolaminates by combined ALD/MLD method, such as TiO_x-self-assembled multilayers (SAMs)/TTIP-H_2O [238], AlO_x-SAMs/Al_2O_3 [239], AlO_x-SAMs/ZnO [239], AlO_x-SAMs/Al_2O_3/AlO_x-SAMs/ZnO [239], ZnO/DEZ-HQ [240], ZnO/DEZ-AP [240], ZnO/DEZ-ODA [240], Al_2O_3/AlEG alloy [241,242], 1,4-phenylene diisocyanate (PDIC)-ethylenediamine (ED)/PDIC-2,2'-thiobis(ethylamine) (TBEA)/PDIC-ED [243], self-assembled organic layers (SAOLs) and Al_2O_3 [244], titanium oxide cross-linked polydiacetylene (TiOPDA)-TiO_2 [245], hafnicone and HfO_2/Hafnicone [161]. For example, Lee et al. in 2007 [238] first prepared TiO_x-SAMs/TiO_2 nanolaminate films. ALD TiO_2-coated Si(100) substrate was alternatively exposed in 7-octenyltrichlorosilane (7-OTS) and H_2O to produce an alkene-terminated self-assembled monolayer (SAM). Then, O_3 was introduced to transfer the terminal C=C groups in SAM into carboxylic groups. Finally, titanium hydroxyl groups were generated by sequentially dosing titanium isopropoxide (TTIP) and H_2O. Lee et al. [241] fabricated the alucone alloys using different ratios of Al_2O_3:alucone (1:1 and 3:1). Based on different alucone contents, hardness and elastic modulus of the alucone alloys changed from 1.0 ± 0.1 GPa to 13.0 ± 0.2 GPa and 21 ± 8 to 198 ± 8 GPs, respectively. Therefore, mechanical properties of these alloy films such as hardness and elastic modulus can be finely tuned by adjusting the relative number of ALD cycle and MLD cycle in the reaction sequence.

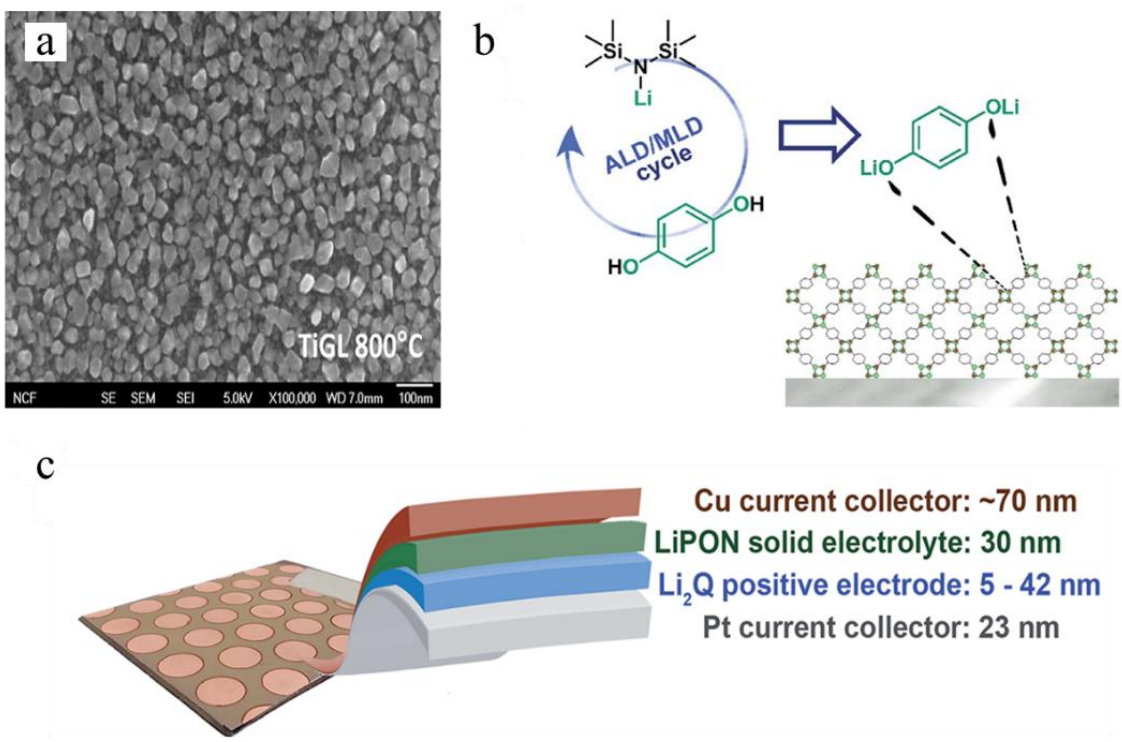

Figure 8. (a) SEM image of a titanicone MLD films using $TiCl_4$ and glycerol after pyrolysis under argon at 800 ℃ for 1 h [227]. Reprinted (adapted) with permission from Ref. [227]. Copyright (2013) American Chemical Society; (b) ALD/MLD process for synthesizing Li_2Q thin films. (c) Schematic presentation of the Li_2Q/LiPON/Cu cells used to evaluate the electrochemical performance of Li_2Q. The in situ Li negative electrode is electroplated on the Cu current collector upon the first charge of the cell [236]. Reprinted (adapted) with permission from Ref. [236]. Copyright (2018) Royal Society of Chemistry.

4.4. 3D NMs

MLD can be used to prepare organic–inorganic hybrid material on 3D substrate using precursors of organometal and organic alcohol. For example, Hall et al. [157] employed MLD to deposit zircone on nanoporous alumina at 150 ℃ using ZTB and EG as precursors. The nanoporous alumina was prepared by a two-step anodization in 0.3 M sulfuric acid solution (0 ℃, 25 V), where an alumina etching process was conducted to separate the first (12 h) and the second anodization step (20 h) (see Figure 9a). SEM showed the cross section of the zircone-coated nanoporous alumina with obliterated pores at the front side (see Figure 9b) and open pores at the back side (see Figure 9c).

Another 3D nanostructure is metal–organic framework (MOF). MOF is composed of inorganic metal-based clusters and organic linkers to generate highly porous crystalline structures [246,247]. MOF displays high thermal stability [248], high surface area [248], and unrivalled versatility in pore composition and geometry [249]. The preparation of MOF using atomic and molecular layer deposition has been spurred [246,247,250,251], due to the precise control over the thickness at molecular level. For instance, Salmi et al. in 2013 [252] first deposited MOF-5 at 225–350 ℃ using zinc acetate ($ZnAC_2$) and 1,4-benzenedicarboxylic acid (BDC) as precursors. The as-deposited films

were initially amorphous and solid. However, following by exposure in moist air at room temperature and then solvothermal treatment in dimethylformamide (DMF) at 150 ℃, the crystalline and porous MOF-5 phase was obtained. This paper indicated that post-treatment was an effective method for the crystallization of porous MOF. In another work, Ahvenniemi et al. [246] fabricated a highly crystalline copper(II)terephthalate (Cu-TPA) MOF on p-type Si (100) substrates at 180–280 ℃ by MLD method using $Cu(thd)_2$ (copper 2,2,6,6-tetramethyl-3,5-heptanedione) and terephthalic acid (TPA) as precursors. The researchers emphasized that the conformity of MOF films via MLD on different substrates or architectures was owed to its surface saturation growth.

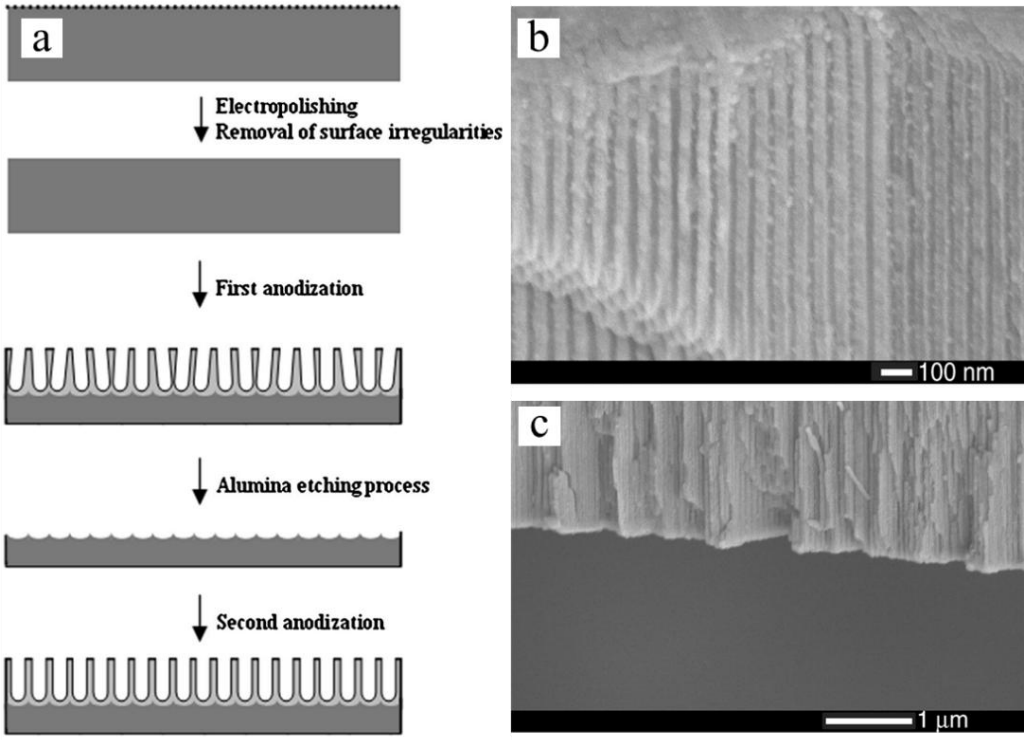

Figure 9. (a) Preparation of highly ordered nanoporous alumina. (b) Cross section SEM of the front side, showing the closure of the pores. (c) Cross section SEM of the back side with open pores [157]. Reprinted (adapted) with permission from Ref. [157]. Copyright (2014) Springer Nature.

5. Promising applications

5.1. Surface engineering

ALD/MLD thin film techniques hold a great promise for the surface modification, allowing for new strategies in the modification of chemical and physical properties of nanoscale materials and the synthesis routes to novel nanostructures, due to its capability of precisely controllable thickness and conformal coverage. Different nanostructures (i.e., nanopores [253,254], nanowires [116,190], nanotubes [191,255], nanopatterns [256–258], and nanolaminates [259]) have been modified via

ALD thin films for various applications (i.e., optical devices [184,215,218,260,261], wettability [262,263], and mechanical applications [259]).

Highly conformal and uniform ALD coatings can contribute significantly to the photonic band gap properties for attaining high performance optical devices. Park et al. [184] investigated the well-ordered TiO_2 nanobowls via ALD for optical properties. This unique nanostructure with 58 nm shell thickness assisted YAG:Ce CPP-capped LED (see Figure 10a) to achieve the maximum luminous efficacy of 119.0 lm/W at 350 mA with an optimized nanobowl structure (see Figure 10b), which is 54% higher than that of a conventional CPP-capped LED (77.2 lm/W). Zaitsu et al. [215] demonstrated the controllable refractive index of ALD Al_2O_3 and TiO_2 2D nanolaminates by tuning the TiO_2 sublayer thickness in the stack. The refractive index of 1.870 to 2.318 was found as a linear proportion to the TiO_2 sublayer thickness varied from 2.0 to 39 Å while Al_2O_3 sublayer remained 5.5 Å thickness. They pointed out that this ALD 2D nanolaminate would be applicable to advanced spectral performance in optical filters with extremely thin layers. Furthermore, King et al. [218] developed ALD 3D TiO_2/ZnS:Mn/TiO_2 inverse opal structures through a combination of inverse opal photonic crystals and atomic layer deposition (ALD). The novel 3D nanostructure of highly crystalline ALD thin films attained full refractive index and strong photoluminescence. These above studies have provided the strong confirmation of the enhanced optical properties in ALD nanostructures.

Wetting property describes the ability of a liquid to sustain on a solid surface, resulting from surface chemistry, roughness and geometry. ALD thin film technique can modify the surface chemistry for the sake of tuning wetting property. Halbur [262] applied ALD Al_2O_3 coating on flexible polytetrafluoroethylene (PTFE) substrate to control the surface energy and wetting properties for the application of aqueous-based nanoparticle inks. PTFE substrates with 175 cycles of ALD Al_2O_3 coating exhibited uniform Ag nanoparticle distribution when ink dried, while the coffee-ring effect for nanoparticle distribution was found on the bare PTFE substrate. The researchers reported that the wettability of Al_2O_3 coated PTFE could be precisely controlled by tuning the Al_2O_3 layer thickness. Hydrophobicity with over 100 ° water contact angle (WCA) was observed for less than 100 ALD cycles, while a sudden change to superhydrophilicity of 0 ° WCA occurred right after 100 ALD cycles. This work addressed that the dramatical improvement of ALD Al_2O_3 coating on uniform distribution of nanoparticle ink casted or printed on PTFE substrate for flexible electronic applications. Dafinone et al. [263] demonstrated both superhydrophilicity (<5 ° water contact angle) of ALD Al_2O_3 coated on inorganic TiO_2/SiO_2 and organic polycarbonate nanoparticle films with a post-treatment of O_2 plasma. The subsequent oxygen plasma treatment essentially removed organic residues from precursors to render the surface superhydrophilicity.

The combined ALD/MLD also demonstrated the modified wetting properties. Gong et al. [264] investigated the combined effects of ALD Al_2O_3 and MLD alucone layers on wettability of the polydimethylsiloxane (PDMS) and Si wafer surface. They first found that 100 cycles of ALD Al_2O_3 layer formed a hydrophilic PDMS surface and hydrophilic Si wafer surface, but after storing for 48 h and 24 h in ambient air they lost the hydrophilicity. Whereas, 200 MLD cycles of alucone on Si wafer led to a durable hydrophilic surface with a low contact angle of 10–30 ° for more than 72 h (see Figure 10c). Then, the researchers combined 100 cycles of Al_2O_3 sublayer on PDMS and 100 cycles of alucone lay on the top, which exhibited the durable hydrophilic surface with a low contact angle of ~20 ° for 200 h in air (see Figure 10d). Therefore, the combination of sequential vapor infiltration

with ALD or MLD on PDMS was effective in engineering and tailoring the chemical properties of surface.

In addition, ALD has been widely recognized as a method to mechanically reinforce nanoparticle thin films on inorganic and organic substrates, due to low-temperature deposition and precisely controllable layer thickness. Dafinone et al. [263] investigated the mechanical enhancement of ALD Al_2O_3 coated 0D TiO_2/SiO_2 nanoparticle films. The dramatically increasing elastic modulus and hardness of Al_2O_3-coated TiO_2/SiO_2 films on Si wafers were confirmed with increasing the number of ALD cycle. For example, the use of 15 ALD Al_2O_3 cycles enhanced 4 times for the elastic modulus and 8 times for the hardness of TiO_2/SiO_2 films (see Figure 10e). They also addressed that the ability of low-temperature ALD would be essential to reinforce mechanical properties on organic materials, like polymers and plastics. In addition, Doll et al. [265] studied mechanical properties of 140 nm 2D ZnO/ZrO_2 nanolaminate coating on silicon substrates fabricated via ALD. The nanolaminate contained 8 bilayers of 10 nm ZnO and 7nm ZrO_2 sublayers. As-grown (0002) ZnO crystalline textures improved good tribological properties, and the crystalline ZrO_2 sublayers relatively high toughness acted as a load bearing layer to resist high load and as a pathway to dissipate energy to suppress delamination between the bilayers. Romanes [259] investigated the ALD films metal oxides, 2D ZnO/Al_2O_3 nanolaminates and ZrO_2 thin films, as the solid lubricants at room temperatures. They revealed that a significant enhancement in friction and wear performance was obtained for ALD-grown thin films. Low friction and wear are significantly demanded for precise devices of high aspect-ratio, like microelectromechanical (MEMS) devices.

Several studies have devoted to enhanced mechanical properties by MLD or combined ALD/MLD prepared films, such as Al_2O_3/alucone/Al_2O_3 [266], alucone film (TMA-EA-MA) [267], polyurea [234], ALGL [155], ZnGL [155] and TiGL [155]. Miller et al. [266] studied the mechanical properties of Al_2O_3/AlEG/Al_2O_3 nanolaminates prepared at 155 ℃ on polyethylene naphthalate substrates. The fabricated nanolaminates exhibited different ratios of each layer thickness of 10/3/10 nm, 25/15/25 nm (see Figure 10f), 25/3/25 nm and 25/192/25 nm respectively. Compared with the pure components, the nanolaminates delivered the reduced critical strains at fracture because of the low toughness of the TMA + EG alucone films. Miller et al. [267] also investigated the thermomechanical properties of "AB" (TMA-EG) and "ABC" (TMA-EA-MA) alucone films, respectively. The researchers found that the TMA-EG alucone exhibited the elastic modulus of 36.8 ± 5.6 GPa and the Berkovich hardness of 0.47 ± 0.07 GPa, both of which are higher than that of the TMA-EA-MA alucone films (modulus: 13.2 ± 5.0 GPa and hardness: 0.27 ± 0.10 GPa). Besides, AB alucone exhibited thermal expansion coefficients of 12.6 ppm/℃ during heating and 7.1 ppm/℃ during cooling. Therefore, MLD enabled the tailoring of the thermomechanical properties of the coatings. In addition, MLD coatings have enhanced the mechanical properties of 1D MWCNTs. Chen et al. [234] improved chemical compatibility between MWCNT and the polyurethane matrix using MLD polyurea coatings, leading to the enhanced mechanical tensile strength of 50% and elastic modulus of 152%. This can be explained by the following two reasons: (i) better dispersion and interfacial adhesion modified by MLD PU coatings and (ii) urea couplings between MLD polyurea layers and polyurethane polymer matrix. Moreover, Brown et al. [155] discovered that the MLD coatings of alucones (precursors: TMA/GL and TMA/EG), titanicone (precursors: $TiCl_4$/GL), and zincone (precursors: DEZ/GL) could significantly improve the Young's Modulus of MWCNTs. Compared with the pristine CNTs, the MLD coatings exhibited a dramatical decrease in failure strain,

a modest improvement in ultimate tensile strength, and a huge increase in Young's Modulus by a factor ranging from 4.3 (for AlGL) to 13.5 (for AlEG).

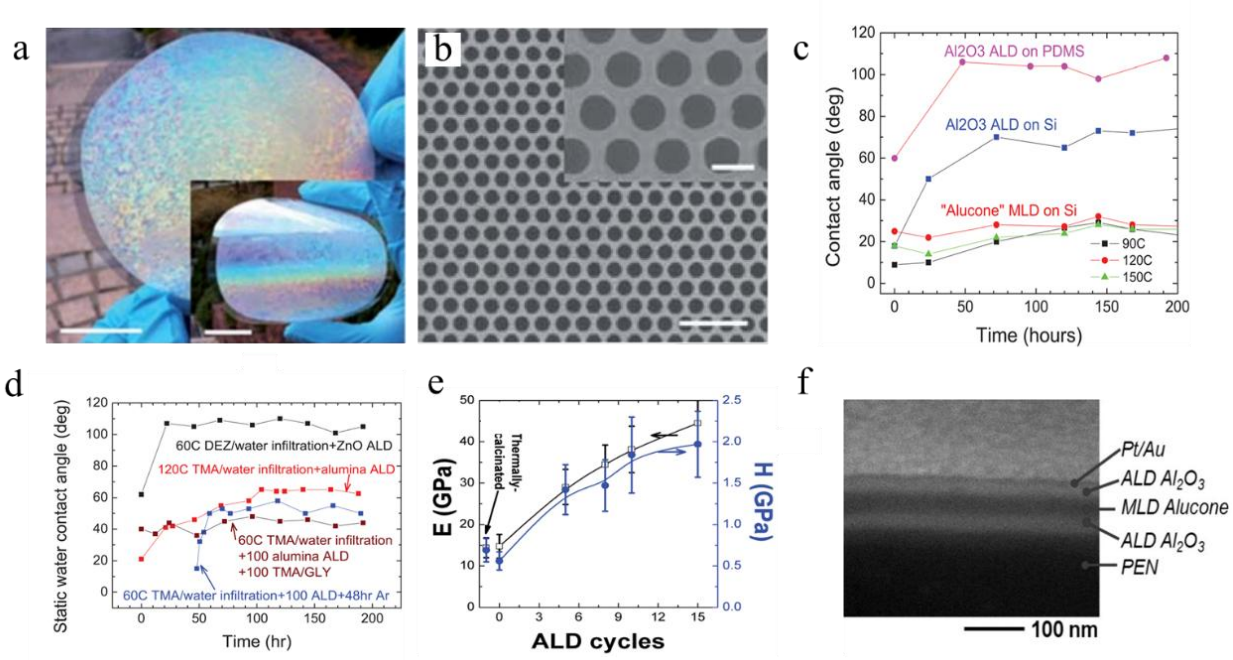

Figure 10. (a) Photographs of a PET substrate with the enhanced optical property, modified by the triangularly patterned 2D TiO_2 nanobowl structure (lattice constant ¼ 580 nm), and the inset shows a picture of bended PET substrate with a nanobowl structure. (b) Top-view FE-SEM images of the 2D TiO_2 nanobowl structure fabricated on PET substrate under low magnification and high magnification (insets) [184]. Reprinted (adapted) with permission from Ref. [184]. Copyright (2013) Royal Society of Chemistry; (c) Water contact angle behavior measured over time for 100 ALD cycles of Al_2O_3 on PDMS and Si wafer at 120 ℃, and Si wafers coated with 200 cycles alucone MLD at 90, 120 and 150 ℃. (d) Water contact angle behavior measured over time for PDMS films with various vapor infiltration and ALD/MLD surface treatments [264]. Reproduced from [264] with the permission of the American Vacuum Society; (e) Nanoindentation results as a function of ALD cycles for TiO_2/SiO_2 nanoparticle films on Si wafers [263]. Reprinted (adapted) with permission from Ref. [263]. Copyright (2011) American Chemical Society; (f) Cross section of multilayer coating on PEN, exhibiting the reduced critical strain [266]. Reproduced from [266] with the permission of AIP Publishing.

5.2. Catalysis

Catalysis is an important approach to selectively increase the chemical reactivity using catalysts, typically noble metals. ALD has gained many interests as a promising method for synthesis of catalyst materials. Due to its self-limiting surface reaction, ALD is capable of designing and modifying catalysts at the nanoscale via precisely control composition. Sun et al. [268] first reported the single-atom catalysis of isolated Pt atoms anchored to graphene nanosheet via ALD. Pt single

atoms and sub-nanometer clusters (see Figure 11a) were ALD-deposited uniformly on graphene at 450 ℃ using $MeCpPtMe_3$ (held at 65 ℃) and O_2 as precursors. The researchers demonstrated that ALD was advantageous on precisely controlling the morphology, size, density and loading of Pt on graphene by tuning the number of ALD cycles. The catalytic performance examined the higher methanol oxidation reaction (MOR) activity and superior CO tolerance, in comparison with conventional larger-scale Pt/C catalysts (see Figure 11b). Sun et al. [268] interpreted that the excellent catalytic performance was attributed to the single Pt atoms. In addition, Christensen et al. [269] fabricated Ru–Pt bimetallic nanoparticle catalysts via ALD for fuel cell applications. Ru–Pt nanoparticles of ~1.2 nm diameter was deposited on Al_2O_3 nanospheres by two ALD steps of Ru(DER) (kept at 80 ℃)/O_2 and Pt(MeCp)Me_3 (kept at 50 ℃)/O_2. MOR measurement revealed that an over 90% conversion efficiency was obtained for ALD Ru–Pt nanostructured catalysts at the temperature of 270 ℃, which was almost double that of physical mixture of monometallic Ru and Pt catalysts. The authors indicated that the steep temperature dependence implied high activation energy for the bimetallic catalysts and also supported bimetallic nanoparticles yielded by ALD synthesis method.

For MLD-synthesized catalysts, Ishchuk et al. [270] deposited TiEG films on planar SiO_2 membrane (40 nm thick) by MLD using $TiCl_4$ and EG as precursors at 100–120 ℃. The enhanced photocatalytic activity of annealed TiEG films at 650 ℃ was enabled by the co-existing amorphous-crystalline state. To clarify, amorphous state provided accessible adsorption sites, and crystalline state were photocatalytic active. This work indicated that MLD was a unique method to prepare nanometric hybrid materials for high photocatalytic activity. Similarly, Sarkar et al. [271] employed MLD to prepare nonstoichiometric oxides for tailoring the reactivity of metal oxide photocatalysis. Reactivity of TiEG films annealed at 650 ℃ for photodegradation of terephthalic acid (TPA) was highly dependent on the deep valence band. Different from the two-step MLD process in the above discussions, Chen et al. [160] employed a four-step MLD process of $TiCl_4$-ethanolamine (EA)-malonyl chloride (MC)-EA at 100 ℃ on carbon nanocoils (CNCs), followed by a thermal treatment at 600 ℃ in Ar/H_2 to receive porous N-doped TiO_2/amorphous-carbon composite on CNCs. Through annealing at 350 ℃ in air to remove the amorphous carbon and increase the surface area, the porous N-doped TiO_2@CNCs treated at 350 ℃ exhibited the best catalytic efficiency for photodegradation of methylene blue (MB) in air (see Figure 11c) under visible light irradiation ($\lambda \geq 420$ nm).

In addition, catalysts suffered from the irreversible deactivation in catalytic processes, induced by various mechanisms, such as poisoning, coking and fouling, sintering, and attrition [272]. ALD has shown its ability to inhibit nanoparticle mobility of metal catalysts by the encapsulation from a conformal ALD coating, which stabilizes catalysts for an extended lifetime. O'Neill et al. [273] demonstrated a stabilization approach for copper catalysts via ALD. ALD Al_2O_3 coating wereas deposited onto oxidized copper nanoparticles using the precursors of TMA and H_2O. Then, a heat treatment for as-synthesized nanocomposite was conducted at 973 K to yield porosity in the encapsulation, in order to provide access to the underlying copper particles. The stabilized catalytic behavior indicated that sintering and leaching issues located at edges, corners, and defects of copper atoms were effectively suppressed by the separation from Al_2O_3-coated Cu nanoparticles. Similarly, Feng et al. [274] reported the enhanced stability and reactivity of Pd nanoparticle catalysts via ALD Al_2O_3 coating using TMA and H_2O. MOR results indicated that nearly 100% methanol conversion efficiency at 270 ℃ catalytic temperature for 6 h had been obtained for the 1–16 cycles of Al_2O_3 coating on Pd nanoparticle (see Figure 11d). Remarkably, Pd nanoparticle with only 1 cycle of Al_2O_3

coating maintained the nearly same size of fresh Pd nanoparticles after 6 h MOR catalytic process, observed through STEM (see Figure 11e). Feng et al. [274] addressed that a single ALD Al_2O_3 cycle (~0.1 nm) was sufficient to suppress sintering issues of Pd nanoparticles during catalytic process. Overall, these useful strategies for catalysis stabilization have been demonstrated to substantially improve the conversion efficiency and reduce the high cost of the use of noble metals in fuel cells and other catalysis applications.

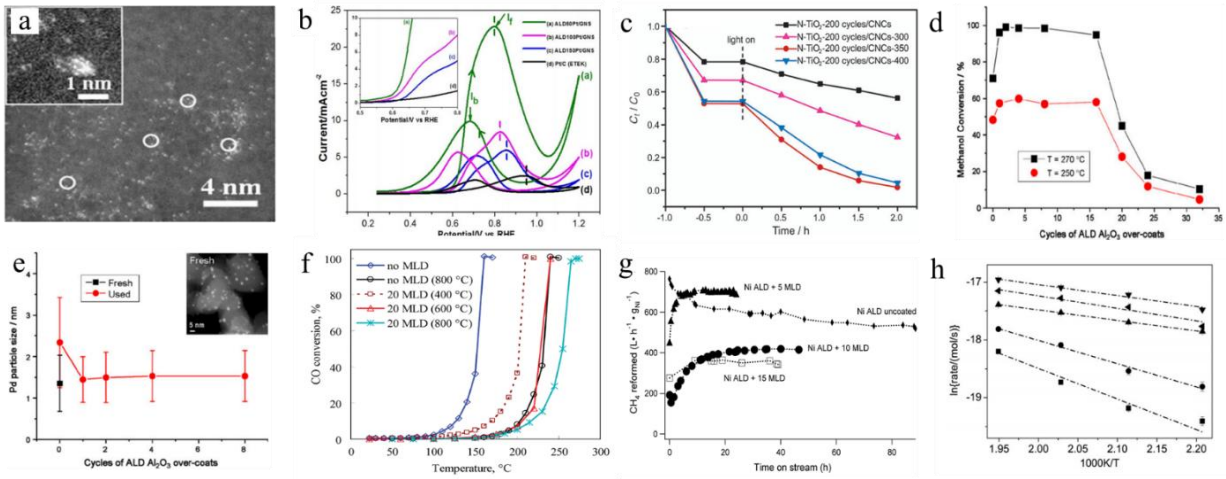

Figure 11. (a) HAADF-STEM images of Pt/GNS samples with 50 ALD cycles, showing the single-atom Pt and sub-nanometer Pt cluster, and (b) CVs of methanol oxidation on ALD50Pt/GNS, ALD100Pt/GNS, ALD150Pt/GNS, and Pt/C, where ALD50Pt/GNS is over 9.5 times higher activity for MOR than of Pt/C catalyst [268]. Reprinted (adapted) with open access permission under a Creative Commons Attribution-NonCommercial-NoDerivs 3.0 Unported License from Ref. [268]. Copyright (2013) Scientific Reports; (c) Photocatalytic degradation of MB under visible light irradiation monitored as the normalized concentration change versus irradiation time for different samples (C_t is the concentration of MB at the irradiation time t and C_0 is the initial concentration) [160]. Reprinted (adapted) with permission from Ref. [160]. Copyright (2013) John Wiley and Sons; (d) Methanol conversion for Pd catalysts with 0–32 cycles of ALD Al_2O_3 coating in the MOR carried out at 250 and 270 ℃, and (e) Pd particle size for fresh (as-prepared) and used (MOR at 270 ℃) catalysts versus number of ALD Al_2O_3 cycles. Inset shows representative STEM image of fresh Pd sample without Al_2O_3 over-coat [274]. Reprinted (adapted) with permission from Ref. [274]. Copyright (2011) American Chemical Society; (f) Effects of the sintering temperature and the alumina layer via MLD on the CO oxidation reaction [275]. Reprinted (adapted) with permission from Ref. [275]. Copyright (2011) Springer Nature; (g) Dry reforming rates at 973 K for uncoated Ni ALD catalyst and the same catalyst coated with 5, 10, and 15 MLD layers [276]. Reprinted (adapted) with permission from Ref. [276]. Copyright (2014) American Chemical Society; (h) Arrhenius plot for GVL synthesis from LA hydrogenation on Cu/CNTs (■), Cu–Zn40MLD (●), Cu–Zn80MLD (▲), Cu–Zn120MLD (▼), and Cu–Zn160MLD (◀) [277]. Reprinted (adapted) with permission from Ref. [277]. Copyright (2015) American Chemical Society.

MLD has also shown an ability for the sake of catalysis stabilization. In this regard, Liang et al. [275] have protected Pt nanoparticles using a thermally stable, highly dispersed and ultrathin porous alucone shell (1–4 nm). Prior to the deposition of TMA-EG alucone films, Pt nanoparticles were deposited on mesoporous silica particles at 320 ℃ by ALD in a fluidized-bed reactor (FBR) using methylcyclopentadienyl-(trimethyl) platinum(IV) ($MeCpPtMe_3$) and O_2 as precursors. After holding the catalysts at 400, 600 and 800 ℃ for 4 h in air, the porous alucone layer significantly reduced the sintering rate of Pt nanoparticles, especially for thicker alucone films. The 20 MLD cycles coated catalyst annealed at 800 ℃ exhibited less catalytical activity of oxidizing CO than that annealed at 600 ℃ (see Figure 11f), due to the amorphous-to-γ alumina transition. Subsequently, Gould et al. [276] stabilized Ni catalyst using a porous alumina layer, which was prepared by calcinating the TMA-EA-methane (MA) alucone films in O_2 gas. Dry reforming activity of methane and stability at 700 ℃ of the catalysts were evaluated. The 5 MLD-layer modified catalyst reached steady state faster and higher than the 10 MLD-layer modified catalyst (see Figure 11g), resulted from the increased Ni surface area by the alumina pores expansion and NiO reduction under reaction conditions. The 10 MLD-layer modified catalyst was stable even after repeated calcinations and reductions (108 h). Moreover, Zhang et al. [277] employed a four-step ABCB MLD method (DEZ/1,4-Phenylene diisocyanate (PPDI)/ethanediamine (EDA)/PPDI) to deposit Zn-hybrid films on Cu@CNTs composites. Followed by a calcination at 300 ℃ in air and a reduction at 300 ℃ in H_2/N_2 gas, the resultant Cu–ZnO@CNTs composites obtained from 120 MLD cycles delivered the highest efficiency and stability in hydrogeneration catalysis (see Figure 11h), resulted from the Cu–ZnO interaction and the suppressing of Cu NPs sintering.

5.3. Batteries

Rechargeable batteries as electrical energy storage (EES) devices play important roles in mitigating the stress of sharply increasing energy demands, deficient energy resources [278–281], environmental pollution [282–284] and global warming issue [285–288]. LIBs as the promising EES devices have been widely applied in portable electronics and electric vehicles, owing to their high energy density. Nevertheless, conventional LIBs suffered from the stringent requirements of higher capacity, higher power, and better cyclability. ALD/MLD nanostructures have been targeted as a solution to improve batteries performance since the past few years, due to their conformal and ultrathin films (1–100 nm) in complex structures with precise growth control [117]. The importance of ALD [20,166–172] and MLD [142,143,146,243,289–294] have been demonstrated in preparing novel electrodes and solid-state electrolytes, protecting the electrode surface, and modifying the separator for LIBs. Many studies related to ALD and MLD have also been devoted to lithium–sulfur batteries [295–297], sodium-ion batteries [114], and lithium air batteries [298].

Protection layers are often used at the interface between electrode materials and electrolyte to enhance the battery performance [117]. Jung et al. [299] demonstrated the surface modification of ALD Al_2O_3 coating on $LiCoO_2$ cathode to enhance the capacity retention of over 80% after 120 charge/discharge cycles, in comparison with 45% of that on bare electrode (see Figure 12a). The significant improvement was attributed to the protection of $LiCoO_2$ from Co dissolution or the mitigation of electrode–electrolyte reactions using an ultrathin Al_2O_3 coating of 4~5 Å. This work demonstrated the great promise of ALD thin films used to protect the interface between electrode and electrolyte and further improve the electrochemical performance of LIBs. Similarly,

Jung et al. [300] deposited ALD Al_2O_3 also on $Li[Li_{0.20}Mn_{0.54}Ni_{0.13}Co_{0.13}]O_2$ cathode, followed by a heat-treatment at 300 ℃ in air. The heat treatment induced the inter-diffusion of atoms between the Al_2O_3 coating and the $Li[Li_{0.20}Mn_{0.54}Ni_{0.13}Co_{0.13}]O_2$ core, leading to better Li^+ ion conductivity through the coating. The resultant cathode exhibited a good cyclability of 50 cycles with high capacity retention. Afterwards, there have been a sharp increase in number of ALD protection coating (i.e., ZrO_2 [301], TiO_2 [302], and SnO_2 [303]) on both cathodes (i.e., $LiMnO_4$ [301] and $LiNi_{0.5}Mn_{1.5}O_4$ [304]) and anodes (i.e., graphene [304], Si [305], and V_2O_5 [306]) of LIBs. For LIB anodes, ALD coating also have the capability of providing accommodation to the huge volume change (i.e., 400% in Si anode [307]) and reducing the formation of solid electrolyte interface [304].

Surface modification via MLD is also effective to improve the performance of LIB and Li–S batteries. Piper et al. [308] deposited 5 nm AlGL films on 0D Si nanoparticles at 140 ℃. This conformal and flexible inorganic–organic hybrid thin film was believed to infiltrate the porous structure of the electrode and covalently bind to surfaces. AlGL coated Si anode exhibited better cycling behavior than the bare Si (see Figure 12b), due to the fact that AlGL films had the passive properties and excellent stability to help mitigate the secondary reactions between the electrolyte and the Si electrode surface. Chen et al. [309] deposited 2D TMA-EG alucone film on lithium metal. This alucone film with high cross-linking structure can effectively mitigate the side interaction between lithium and electrolyte and improve the capacity and Coulombic efficiency of lithium batteries. Besides surface coating on Si nanoparticles and lithium metal, sulfur cathode coated by MLD films was also investigated recently. Li et al. [310] deposited 2D TMA-EG alucone films on carbon/sulfur (i.e., C/S) cathodes to improve the performance of the Li–S battery (see Figure 12c). With a 5-cycle alucone coating, the C/S cathode displayed flat potential plateaus, which demonstrated the high reversibility of the Li–S redox reaction.

Furthermore, the ability to ALD conformality in complex structures is extremely helpful for designing novel nanostructures for battery electrode. Liu et al. [311] applied ALD to synthesize iron phosphate ($FePO_4$) conformally coated on nitrogen-doped carbon nanotubes (NCNTs) by using two ALD steps of Fe_2O_3 (ferrocene/ozone as precursors) and PO_x (trimethyl phosphate/water as precursors) at 200~350 ℃. Even though low discharge capacity of 177 mAh/g in the first cycle, the as-synthesized $FePO_4$@NCNTs exhibited a discharge capacity of 141 mAh/g after 100 cycles and indicated a fairly good cyclability with high capacity retention. Lu et al. [312] reported ALD ZnO (DEZ/H_2O as precursors) on carbon black as a nanostructured anode in LIBs. The nanostructured ZnO anode suppressed large volume change (of 228%) during charge/discharge cycles and mitigated the rapid capacity fading, in comparison with bulk ZnO. A durable cyclability with a high reversible capacity of 1026 mAh/g was retained after 500 cycles. The nanocomposites also presented excellent rate capability with a reversible capacity of 1080 mAh/g at 2000 mA/g. The authors revealed that the strong interfacial molecular bindings in the ALD-synthesized nanocomposites provided stable and robust electrical contact during lithiation and delithiation processes. This approach could be extended to the ALD-synthesis of other metal oxide (i.e., TiO_2 [313] and SnO_2 [303]) based anodes for high power LIBs.

2D nanostructured materials via MLD were also applied in electrode design. Kerckhove et al. [162] deposited tetrakisethylmethylaminovanadium (TEMAV)/EG and TEMAV/GL vanadicone films. Then, the as-deposited films were annealed in He gas to receive amorphous V_2O_5 and carbon composites. Cyclic voltammograms results revealed that the as-resultant V_2O_5@carbon composites exhibited better electrochemical performance than the bulk V_2O_5, in terms of capacity,

rate performance and cyclability. Kerckhove et al. [158] designed another 2D electrode for lithium ion batteries via MLD, using tetrakisdimethylaminotitanium (TDMAT)/GL and TDMAT/EG titanicone films. The as-deposited samples were annealed in air to become anatase TiO_2 phase, while He-annealed samples were amorphous TiO_2 phase. From the electrochemical experiments, anatase and amorphous TiO_2 samples fabricated via this MLD approach both exhibited higher rate capability, compared to their respective anatase and amorphous TiO_2 via ALD processes. Furthermore, Nisula et al. [314] prepared a novel lithium ion battery using high rate-capability anode LiTP with a solid-state electrolyte LiPON via the combined ALD/MLD. The as-prepared LiPON thin film as solid-state electrolyte could avoid instability/dissolution issues of liquid organic electrolytes and also improve the electrical conductivity. The novel LiTP–LiPON battery demonstrated a high capacity retention of 97% with a high rate of 3.2 C after 200 discharge/charge cycles (see Figure 12d).

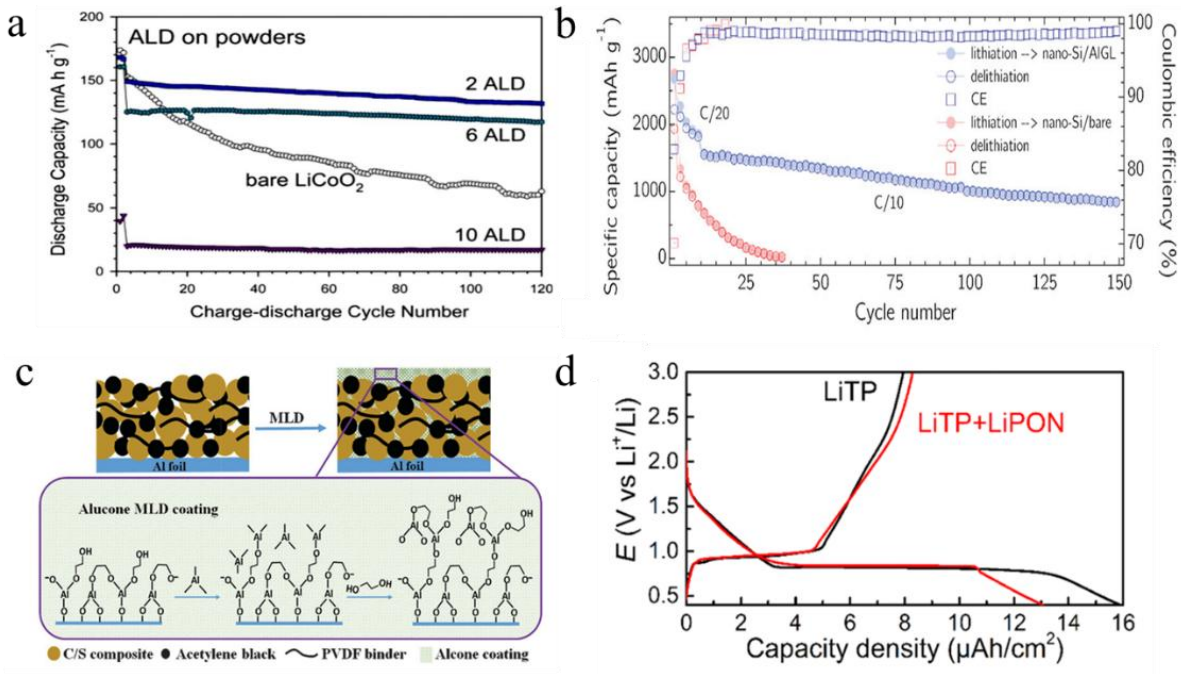

Figure 12. (a) Charge–discharge cycle performance of the bare $LiCoO_2$ powders and the Al_2O_3 ALD-coated $LiCoO_2$ powders using 2, 6, and 10 ALD cycles [299]. Reproduced with permission from Ref. [299]. Copyright (2011) Journal of the Electrochemical Society; (b) Cyclic capacity (circle symbols) and CE (square symbols) of a nano-Si/AlGL anode in comparison with of a nano-Si bare composite electrode. At cycle 150, the nano-Si/AlGL cell shows a specific charge capacity of nearly 900 mAh/g with a CE of 99%, whereas the nano-Si/bare electrode fails after 30 cycles [308]. Reprinted (adapted) with permission from ref. [308]. Copyright (2013) John Wiley and Sons; (c) Schematic illustration of alucone MLD thin film formation as a coating layer applied on a C/S cathode [310]. Reprinted (adapted) with permission from Ref. [310]. Copyright (2014) Royal Society of Chemistry; (d) The initial charge/discharge curves of LiTP (black line) and LiTP–LiPON (red line) recorded using a current density of 0.5 μA/cm^2 (~0.05 C) [314]. Reprinted (adapted) with permission from Ref. [314]. Copyright (2016) American Chemical Society.

6. Conclusions

The miniaturization in nanotechnology requests a facile and high-quality fabrication method for nanostructured materials. To this end, ALD and MLD techniques recently have emerged as the promising fabrication techniques for inorganic, organic, and inorganic–organic hybrid nanostructured materials, due to precise controllability and high conformality at low temperature atomic-scale or molecular-scale deposition. ALD and MLD are both vapor phase methods based on saturating and self-limiting surface reactions using the alternating exposures of different precursors. Our work introduced the necessities of nanostructured materials and the practical capabilities of ALD and MLD, as well as briefly introducing the mechanisms of ALD and MLD. Subsequently, the fabrication strategies via ALD and MLD individually were highlighted to novel nanostructured materials categorized in 0D, 1D, 2D, and 3D structures. Then, we exemplified the applications of ALD and MLD in surface engineering, catalysis, and batteries. With this work, we expect that more solutions will be brought to practical issues by the versatile capabilities of ALD and MLD for nanostructured materials. In this regard, new research efforts have emerged and hopefully will bring forth breakthroughs in many areas. For instance, ALD and MLD have been verified for their versatile capabilities in tailoring interfaces [299,308] and designing nanostructured electrodes for energy devices like rechargeable batteries [311,312]. Recently, there has been an increase number of solid-state electrolytes [236,314] reported by ALD and MLD for these energy systems for improved performance. In addition, the combination of ALD and MLD is becoming a new research thrust for surface engineering, featuring their powerful capabilities for new hybrid materials with desirable properties [259,261,263]. In catalysis, furthermore, ALD and MLD are becoming new techniques for developing high-efficient catalysts, such as single-atom catalysts [268]. Even more, ALD and MLD have been reported for synthesizing structurally 2D materials [315] and 3D MOF [246,252,316]. All these and others not discussed in this work together evidence that ALD and MLD are expanding quickly in their applications with new solutions.

Acknowledgements

Funding for this research was provided by the Center for Advanced Surface Engineering, under the National Science Foundation Grant No. OIA-1457888 and the Arkansas EPSCoR Program, ASSET III.

Conflict of interest

All authors declare no conflicts of interest in this paper.

References

1. Siegel RW (1993) Nanostructured materials-mind over matter. *Nanostruct Mater* 3: 1–18.
2. Moriarty P (2001) Nanostructured materials. *Rep Prog Phys* 64: 297–381.
3. Chen X, Li C, Grätzel M, et al. (2012) Nanomaterials for renewable energy production and storage. *Chem Soc Rev* 41: 7909–7937.
4. Alivisatos AP (1996) Perspectives on the physical chemistry of semiconductor nanocrystals. *J Phys Chem* 100: 13226–13239.

5. Burda C, Chen X, Narayanan R, et al. (2005) Chemistry and properties of nanocrystals of different shapes. *Chem Rev* 105: 1025–1102.
6. Peng L, Fang Z, Zhu Y, et al. (2018) Holey 2D nanomaterials for electrochemical energy storage. *Adv Energy Mater* 8: 1702179.
7. Bottari G, de la Torre G, Guldi DM, et al. (2010) Covalent and noncovalent phthalocyanine–carbon nanostructure systems: synthesis, photoinduced electron transfer, and application to molecular photovoltaics. *Chem Rev* 110: 6768–6816.
8. Lee J, Singer JP, Thomas EL (2012) Micro-/Nanostructured mechanical metamaterials. *Adv Mater* 24: 4782–4810.
9. Fourkas JT (2010) Nanoscale photolithography with visible light. *J Phys Chem Lett* 1: 1221–1227.
10. Biswas A, Bayer IS, Biris AS, et al. (2012) Advances in top-down and bottom-up surface nanofabrication: Techniques, applications & future prospects. *Adv Colloid Interfac* 170: 2–27.
11. Li SP, Peyrade D, Natali M, et al. (2001) Flux closure structures in cobalt rings. *Phys Rev Lett* 86: 1102.
12. Berger S, Gibson J, Camarda R, et al. (1991) Projection electron-beam lithography: A new approach. *J Vac Sci Technol B* 9: 2996–2999.
13. Brétagnol F, Sirghi L, Mornet S, et al. (2008) Direct fabrication of nanoscale bio-adhesive patterns by electron beam surface modification of plasma polymerized poly ethylene oxide-like coatings. *Nanotechnology* 19: 125306.
14. Guo LJ (2004) Recent progress in nanoimprint technology and its applications. *J Phys D Appl Phys* 37: R123–R141.
15. Xie G, Zhang J, Zhang Y, et al. (2009) Fabrication of metal suspending nanostructures by nanoimprint lithography (NIL) and isotropic reactive ion etching (RIE). *Sci China Ser E-Technol Sci* 52: 1181–1186.
16. Chen Y, Ohlberg DA, Li X, et al. (2003) Nanoscale molecular-switch devices fabricated by imprint lithography. *Appl Phys Lett* 82: 1610–1612.
17. Leggett GJ (2006) Scanning near-field photolithography-surface photochemistry with nanoscale spatial resolution. *Chem Soc Rev* 35: 1150–1161.
18. Salaita K, Wang Y, Mirkin CA (2007) Applications of dip-pen nanolithography. *Nat Nanotechnol* 2: 145–155.
19. Dagata JA, Schneir J, Harary HH, et al. (1990) Modification of hydrogen-passivated silicon by a scanning tunneling microscope operating in air. *Appl Phys Lett* 56: 2001–2003.
20. Suntola T, Antson J (1977) Method for producing compound thin films. U.S. Patent 4058430.
21. Kim H, Maeng W (2009) Applications of atomic layer deposition to nanofabrication and emerging nanodevices. *Thin Solid Films* 517: 2563–2580.
22. López T, Recillas S, Guevara P, et al. (2008) Pt/TiO_2 brain biocompatible nanoparticles: GBM treatment using the C6 model in Wistar rats. *Acta Biomater* 4: 2037–2044.
23. Song F, Su H, Han J, et al. (2010) Controllable synthesis and gas response of biomorphic SnO_2 with architecture hierarchy of butterfly wings. *Sensor Actuat B-Chem* 145: 39–45.
24. Weatherspoon MR, Cai Y, Crne M, et al. (2008) 3D rutile titania-based structures with morpho butterfly wing scale morphologies. *Angew Chem* 120: 8039–8041.
25. Zhao Y, He S, Wei M, et al. (2010) Hierarchical films of layered double hydroxides by using a sol–gel process and their high adaptability in water treatment. *Chem Commun* 46: 3031–3033.

26. Bayer I, Biswas A, Tripathi A, et al. (2009) Composite thin films of poly(phenylene oxide)/poly(styrene) and PPO/silver via vapor phase deposition. *Polym Advan Technol* 20: 775–784.
27. Dervishi E, Li Z, Watanabe F, et al. (2009) Thermally controlled synthesis of single-wall carbon nanotubes with selective diameters. *J Mater Chem* 19: 3004–3012.
28. Novoselov KS, Geim AK, Morozov SV, et al. (2005) Two-dimensional gas of massless Dirac fermions in graphene. *Nature* 438: 197–200.
29. Biswas A, Eilers H, Hidden Jr F, et al. (2006) Large broadband visible to infrared plasmonic absorption from Ag nanoparticles with a fractal structure embedded in a Teflon AF® matrix. *Appl Phys Lett* 88: 013103.
30. Mijatovic D, Eijkel JC, van den Berg A (2005) Technologies for nanofluidic systems: top-down vs. bottom-up—a review. *Lab Chip* 5: 492–500.
31. Hobbs RG, Petkov N, Holmes JD (2012) Semiconductor nanowire fabrication by bottom-up and top-down paradigms. *Chem Mater* 24: 1975–1991.
32. Siegel RW (1993) Synthesis, Structure and Properties of Nanostructred Materials, In: Fiorani D, Sberveglieri G, *Fundamental properties of nanostructured materials*, Singapore: World Scientific, 3–19.
33. Yu Z, Tetard L, Zhai L, et al. (2015) Supercapacitor electrode materials: nanostructures from 0 to 3 dimensions. *Energ Environ Sci* 8: 702–730.
34. Kiss L, Söderlund J, Niklasson G, et al. (1999) New approach to the origin of lognormal size distributions of nanoparticles. *Nanotechnology* 10: 25–28.
35. Tang F, Higgins AJ, Goroshin S (2009) Effect of discreteness on heterogeneous flames: propagation limits in regular and random particle arrays. *Combust Theor Model* 13: 319–341.
36. Kim Y, Han JH, Hong BH, et al. (2010) Electrochemical synthesis of CdSe quantum-dot arrays on a graphene basal plane using mesoporous silica thin-film templates. *Adv Mater* 22: 515–518.
37. Wang J, Lin M, Yan Y, et al. (2009) CdSe/AsS core–shell quantum dots: preparation and two-photon fluorescence. *J Am Chem Soc* 131: 11300–11301.
38. Portet C, Yushin G, Gogotsi Y (2007) Electrochemical performance of carbon onions, nanodiamonds, carbon black and multiwalled nanotubes in electrical double layer capacitors. *Carbon* 45: 2511–2518.
39. Lee JY, Hong BH, Kim WY, et al. (2009) Near-field focusing and magnification through self-assembled nanoscale spherical lenses. *Nature* 460: 498–501.
40. Jeevanandam J, Barhoum A, Chan YS, et al. (2018) Review on nanoparticles and nanostructured materials: history, sources, toxicity and regulations. *Beilstein J Nanotech* 9: 1050–1074.
41. Xia H, Feng J, Wang H, et al. (2010) MnO_2 nanotube and nanowire arrays by electrochemical deposition for supercapacitors. *J Power Sources* 195: 4410–4413.
42. Park J, Nalwa KS, Leung W, et al. (2010) Fabrication of metallic nanowires and nanoribbons using laser interference lithography and shadow lithography. *Nanotechnology* 21: 215301.
43. Okada T, Kawashima K, Nakata Y, et al. (2005) Synthesis of ZnO nanorods by laser ablation of ZnO and Zn targets in He and O_2 background gas. *Jpn J Appl Phys* 44: 688–691.
44. Han J, Qin J, Guo L, et al. (2018) Ultrasmall Fe_2GeO_4 nanodots anchored on interconnected carbon nanosheets as high-performance anode materials for lithium and sodium ion batteries. *Appl Surf Sci* 427: 670–679.

45. Yuan W, Qiu Z, Chen Y, et al. (2018) A binder-free composite anode composed of CuO nanosheets and multi-wall carbon nanotubes for high-performance lithium-ion batteries. *Electrochim Acta* 267: 150–160.
46. Li C, Wei G, Wang S, et al. (2018) Two-dimensional coupling: Sb nanoplates embedded in MoS_2 nanosheets as efficient anode for advanced sodium ion batteries. *Mater Chem Phys* 211: 375–381.
47. Tang Q, Su H, Cui Y, et al. (2018) Ternary tin-based chalcogenide nanoplates as a promising anode material for lithium-ion batteries. *J Power Sources* 379: 182–190.
48. Kong X, Wang Y, Lin J, et al. (2018) Twin-nanoplate assembled hierarchical Ni/MnO porous microspheres as advanced anode materials for lithium-ion batteries. *Electrochim Acta* 259: 419–426.
49. Xu F, Liu M, Li X, et al. (2018) Loading of indocyanine green within polydopamine-coated laponite nanodisks for targeted cancer photothermal and photodynamic therapy. *Nanomaterials* 8: 1–16.
50. Li Z, Huang F, Peng B, et al. (2018) A kind of economical, environment-friendly and controllable synthesis of Nb_3O_7F nanowalls and their photocatalytic properties. *Mater Lett* 214: 165–169.
51. Srivastava SK, Kumar V, Vankar VD (2018) Carbon Nanowalls: A potential 2-Dimensional material for field emission and energy-related applications, In: Khan Z, *Nanomaterials and Their Applications*, Part of the Advanced Structured Materials book series, Singapore: Springer, 27–71.
52. Gautam UK, Vivekchand S, Govindaraj A, et al. (2005) GaS and GaSe nanowalls and their transformation to Ga_2O_3 and GaN nanowalls. *Chem Commun* 3995–3997.
53. Park JK, Kang H, Kim JH, et al. (2018) Improvement of electrical properties of carbon nanowall by the deposition of thin film. *J Nanosci Nanotechno* 18: 6026–6028.
54. Khot LR, Sankaran S, Maja JM, et al. (2012) Applications of nanomaterials in agricultural production and crop protection: a review. *Crop Prot* 35: 64–70.
55. Peters RJ, Bouwmeester H, Gottardo S, et al. (2016) Nanomaterials for products and application in agriculture, feed and food. *Trends Food Sci Tech* 54: 155–164.
56. Navrotsky A (2000) Nanomaterials in the environment, agriculture, and technology (NEAT). *J Nanopart Res* 2: 321–323.
57. Paull J (2011) Nanomaterials in food and agriculture: The big issue of small matter for organic food and farming. *Proceedings of the Third Scientific Conference of ISOFAR (International Society of Organic Agriculture Research)*, 28 September–1 October, Namyangju, Korea, 2: 96–99.
58. Magnuson BA, Jonaitis TS, Card JW (2011) A brief review of the occurrence, use, and safety of food–related nanomaterials. *J Food Sci* 76: R126–R133.
59. Ranjan S, Dasgupta N, Chakraborty AR, et al. (2014) Nanoscience and nanotechnologies in food industries: opportunities and research trends. *J Nanopart Res* 16: 2464.
60. Kagan CR (2016) At the nexus of food security and safety: opportunities for nanoscience and nanotechnology. *ACS Nano* 10: 2985–2986.
61. Yao J, Yang M, Duan Y (2014) Chemistry, biology, and medicine of fluorescent nanomaterials and related systems: new insights into biosensing, bioimaging, genomics, diagnostics, and therapy. *Chem Rev* 114: 6130–6178.

62. Solanki A, Kim JD, Lee K (2008) Nanotechnology for regenerative medicine: nanomaterials for stem cell imaging. *Nanomedicine* 3: 567–578.
63. Skoog S, Elam J, Narayan R (2013) Atomic layer deposition: medical and biological applications. *Int Mater Rev* 58: 113–129.
64. Lehner R, Wang X, Marsch S, et al. (2013) Intelligent nanomaterials for medicine: carrier platforms and targeting strategies in the context of clinical application. *Nanomed-Nanotechnol* 9: 742–757.
65. Yao J, Sun Y, Yang M, et al. (2012) Chemistry, physics and biology of graphene-based nanomaterials: new horizons for sensing, imaging and medicine. *J Mater Chem* 22: 14313–14329.
66. Xu B (2009) Gels as functional nanomaterials for biology and medicine. *Langmuir* 25: 8375–8377.
67. Masciangioli T, Zhang W (2003) Peer reviewed: environmental technologies at the nanoscale. *Environ Sci Technol* 37: 102A–108A.
68. Mu L, Sprando RL (2010) Application of nanotechnology in cosmetics. *Pharm Res* 27: 1746–1749.
69. Bowman DM, Van Calster G, Friedrichs S (2010) Nanomaterials and regulation of cosmetics. *Nat Nanotechnol* 5: 92.
70. Musee N (2011) Simulated environmental risk estimation of engineered nanomaterials: a case of cosmetics in Johannesburg City. *Hum Exp Toxicol* 30: 1181–1195.
71. Brauer S, Lem K, Haw J (2009) The markets for soft nanomaterials: cosmetics and pharmaceuticals. *Nano and Green Technology Conference*, 17–19.
72. Raj S, Jose S, Sumod US, et al. (2012) Nanotechnology in cosmetics: opportunities and challenges. *J Pharm Bioallied Sci* 4: 186–193.
73. Harifi T, Montazer M (2015) A review on textile sonoprocessing: a special focus on sonosynthesis of nanomaterials on textile substrates. *Ultrason Sonochem* 23: 1–10.
74. Dawson T (2008) Nanomaterials for textile processing and photonic applications. *Color Technol* 124: 261–272.
75. Butola B, Mohammad F (2016) Silver nanomaterials as future colorants and potential antimicrobial agents for natural and synthetic textile materials. *RSC Adv* 6: 44232–44247.
76. Mahmoud HR, Ibrahim SM, El-Molla SA (2016) Textile dye removal from aqueous solutions using cheap MgO nanomaterials: adsorption kinetics, isotherm studies and thermodynamics. *Adv Powder Technol* 27: 223–231.
77. Lee T, Lee W, Kim S, et al. (2016) Flexible textile strain wireless sensor functionalized with hybrid carbon nanomaterials supported ZnO nanowires with controlled aspect ratio. *Adv Funct Mater* 26: 6206–6214.
78. Pradeep T (2009) Noble metal nanoparticles for water purification: a critical review. *Thin Solid Films* 517: 6441–6478.
79. Theron J, Walker JA, Cloete TE (2010) Nanotechnology and water treatment: Applications and emerging opportunities, In: Cloete TE, De Kwaadsteniet M, Botes M, et al. *Nanotechnology in water treatment applications*, Caister Academic Press, 1–38.
80. Savage N, Diallo MS (2005) Nanomaterials and water purification: opportunities and challenges. *J Nanopart Res* 7: 331–342.

81. Ummartyotin S, Manuspiya H (2015) A critical review on cellulose: from fundamental to an approach on sensor technology. *Renew Sust Energ Rev* 41: 402–412.
82. Yoon H, Jang J (2009) Conducting-polymer nanomaterials for high-performance sensor applications: issues and challenges. *Adv Funct Mater* 19: 1567–1576.
83. Llobet E (2013) Gas sensors using carbon nanomaterials: A review. *Sensor Actuat B-Chem* 179: 32–45.
84. Bai J, Zhou B (2014) Titanium dioxide nanomaterials for sensor applications. *Chem Rev* 114: 10131–10176.
85. Sengupta D, Das P, Mondal B, et al. (2016) Effects of doping, morphology and film-thickness of photo-anode materials for dye sensitized solar cell application—A review. *Renew Sust Energ Rev* 60: 356–376.
86. Sengupta D, Das P, Kasinadhuni U, et al. (2014) Morphology induced light scattering by zinc oxide polydisperse particles: Promising for dye sensitized solar cell application. *J Renew Sustain Ener* 6: 063114.
87. Le Viet A, Jose R, Reddy M, et al. (2010) Nb_2O_5 photoelectrodes for dye-sensitized solar cells: choice of the polymorph. *J Phys Chem C* 114: 21795–21800.
88. Saito M, Fujihara S (2008) Large photocurrent generation in dye-sensitized ZnO solar cells. *Energ Environ Sci* 1: 280–283.
89. Turković A, Orel ZC (1997) Dye-sensitized solar cell with CeO_2 and mixed CeO_2/SnO_2 photoanodes. *Sol Energ Mat Sol C* 45: 275–281.
90. Zheng H, Tachibana Y, Kalantar-zadeh K (2010) Dye-sensitized solar cells based on WO_3. *Langmuir* 26: 19148–19152.
91. Zhang Q, Cao G (2011) Hierarchically structured photoelectrodes for dye-sensitized solar cells. *J Mater Chem* 21: 6769–6774.
92. Law M, Greene LE, Johnson JC, et al. (2005) Nanowire dye-sensitized solar cells. *Nat Mater* 4: 455–459.
93. Martinson AB, Elam JW, Hupp JT, et al. (2007) ZnO nanotube based dye-sensitized solar cells. *Nano Lett* 7: 2183–2187.
94. Schlur L, Carton A, L évêque P, et al. (2013) Optimization of a new ZnO nanorods hydrothermal synthesis method for solid state dye sensitized solar cells applications. *J Phys Chem C* 117: 2993–3001.
95. Ameen S, Akhtar MS, Song M, et al. (2012) Vertically aligned ZnO nanorods on hot filament chemical vapor deposition grown graphene oxide thin film substrate: solar energy conversion. *ACS Appl Mater Inter* 4: 4405–4412.
96. Guo D, Wang J, Cui C, et al. (2013) $ZnO@TiO_2$ core-shell nanorod arrays with enhanced photoelectrochemical performance. *Sol Energy* 95: 237–245.
97. Chen H, Zhang T, Fan J, et al. (2013) Electrospun hierarchical TiO_2 nanorods with high porosity for efficient dye-sensitized solar cells. *ACS Appl Mater Inter* 5: 9205–9211.
98. Roy P, Kim D, Lee K, et al. (2010) TiO_2 nanotubes and their application in dye-sensitized solar cells. *Nanoscale* 2: 45–59.
99. Zhang Q, Cao G (2011) Nanostructured photoelectrodes for dye-sensitized solar cells. *Nano Today* 6: 91–109.

100. Lee CS, Kim JK, Lim JY, et al. (2014) One-step process for the synthesis and deposition of anatase, two-dimensional, disk-shaped TiO_2 for dye-sensitized solar cells. *ACS Appl Mater Inter* 6: 20842–20850.
101. Lin J, Peng Y, Pascoe AR, et al. (2015) A Bi-layer TiO_2 photoanode for highly durable, flexible dye-sensitized solar cells. *J Mater Chem A* 3: 4679–4686.
102. Shanmugam M, Jacobs-Gedrim R, Durcan C, et al. (2013) 2D layered insulator hexagonal boron nitride enabled surface passivation in dye sensitized solar cells. *Nanoscale* 5: 11275–11282.
103. Alivov Y, Fan Z (2009) Efficiency of dye sensitized solar cells based on TiO_2 nanotubes filled with nanoparticles. *Appl Phys Lett* 95: 063504.
104. Mahmood K, Kang HW, Munir R, et al. (2013) A dual-functional double-layer film with indium-doped ZnO nanosheets/nanoparticles structured photoanodes for dye-sensitized solar cells. *RSC Adv* 3: 25136–25144.
105. Choi SY, Mamak M, Coombs N, et al. (2004) Thermally stable two-dimensional hexagonal mesoporous nanocrystalline anatase, meso-nc-TiO_2: Bulk and crack-free thin film morphologies. *Adv Funct Mater* 14: 335–344.
106. Shchukin DG, Caruso RA (2004) Template synthesis and photocatalytic properties of porous metal oxide spheres formed by nanoparticle infiltration. *Chem Mater* 16: 2287–2292.
107. Iwasaki M, Davis SA, Mann S (2004) Spongelike macroporous TiO_2 monoliths prepared from starch gel template. *J Sol-Gel Sci Techn* 32: 99–105.
108. Caruso R, Schattka J (2000) Cellulose acetate templates for porous inorganic network fabrication. *Adv Mater* 12: 1921–1923.
109. Chen D, Cao L, Huang F, et al. (2010) Synthesis of monodisperse mesoporous titania beads with controllable diameter, high surface areas, and variable pore diameters (14–23 nm). *J Am Chem Soc* 132: 4438–4444.
110. Cavallo C, Di Pascasio F, Latini A, et al. (2017) Nanostructured semiconductor materials for dye-sensitized solar cells. *J Nanomater* 2017: 5323164.
111. Scrosati B (2000) Recent advances in lithium ion battery materials. *Electrochim Acta* 45: 2461–2466.
112. Goodenough JB, Park K (2013) The Li-ion rechargeable battery: a perspective. *J Am Chem Soc* 135: 1167–1176.
113. Sun Q, Lau KC, Geng D, et al. (2018) Atomic and molecular layer deposition for superior lithium–sulfur batteries: strategies, performance, and mechanisms. *Batteries Supercaps* 1: 41–68.
114. Meng XB (2017) Atomic-scale surface modifications and novel electrode designs for high-performance sodium-ion batteries via atomic layer deposition. *J Mater Chem A* 5: 10127–10149.
115. Zhu C, Han K, Geng D, et al. (2017) Achieving high-performance silicon anodes of lithium-ion batteries via atomic and molecular layer deposited surface coatings: an overview. *Electrochim Acta* 251: 710–728.
116. Knez M, Nielsch K, Niinistö L (2007) Synthesis and surface engineering of complex nanostructures by atomic layer deposition. *Adv Mater* 19: 3425–3438.
117. Knoops H, Donders M, Van De Sanden M, et al. (2012) Atomic layer deposition for nanostructured Li-ion batteries. *J Vac Sci Technol A* 30: 010801.
118. George S, Ott A, Klaus J (1996) Surface chemistry for atomic layer growth. *J Phys Chem* 100: 13121–13131.
119. Suntola T (1992) Atomic layer epitaxy. *Thin Solid Films* 216: 84–89.

120. Kucheyev S, Biener J, Wang Y, et al. (2005) Atomic layer deposition of ZnO on ultralow-density nanoporous silica aerogel monoliths. *Appl Phys Lett* 86: 083108.
121. Zhang W, Dong J, Li C, et al. (2015) Large scale synthesis of pinhole-free shell-isolated nanoparticles (SHINs) using improved atomic layer deposition (ALD) method for practical applications. *J Raman Spectrosc* 46: 1200–1204.
122. Yao Z, Wang C, Li Y, et al. (2015) AAO-assisted synthesis of highly ordered, large-scale TiO_2 nanowire arrays via sputtering and atomic layer deposition. *Nanoscale Res Lett* 10: 166.
123. Klaus J, George S (2000) Atomic layer deposition of SiO_2 at room temperature using NH_3-catalyzed sequential surface reactions. *Surf Sci* 447: 81–90.
124. Mackus AJ, Garcia-Alonso D, Knoops HC, et al. (2013) Room-temperature atomic layer deposition of platinum. *Chem Mater* 25: 1769–1774.
125. Kot M, Das C, Wang Z, et al. (2016) Room-temperature atomic layer deposition of Al_2O_3: Impact on efficiency, stability and surface properties in perovskite solar cells. *ChemSusChem* 9: 3401–3406.
126. Lim BS, Rahtu A, Gordon RG (2003) Atomic layer deposition of transition metals. *Nat Mater* 2: 749–754.
127. Tynell T, Karppinen M (2014) Atomic layer deposition of ZnO: a review. *Semicond Sci Tech* 29: 043001.
128. Meng X, Geng D, Liu J, et al. (2011) Controllable synthesis of graphene-based titanium dioxide nanocomposites by atomic layer deposition. *Nanotechnology* 22: 165602.
129. Wind R, George S (2009) Quartz crystal microbalance studies of Al_2O_3 atomic layer deposition using trimethylaluminum and water at 125 ℃. *J Phys Chem A* 114: 1281–1289.
130. Becker JS, Kim E, Gordon RG (2004) Atomic layer deposition of insulating hafnium and zirconium nitrides. *Chem Mater* 16: 3497–3501.
131. Klug JA, Becker NG, Groll NR, et al. (2013) Heteroepitaxy of group IV–VI nitrides by atomic layer deposition. *Appl Phys Lett* 103: 211602.
132. Han X, Liu Y, Jia Z, et al. (2013) Atomic-layer-deposition oxide nanoglue for sodium ion batteries. *Nano Lett* 14: 139–147.
133. Lee HJ, Seo HO, Kim DW, et al. (2011) A high-performing nanostructured TiO_2 filter for volatile organic compounds using atomic layer deposition. *Chem Commun* 47: 5605–5607.
134. Pore V, Hatanpaa T, Ritala M, et al. (2009) Atomic layer deposition of metal tellurides and selenides using alkylsilyl compounds of tellurium and selenium. *J Am Chem Soc* 131: 3478–3480.
135. Wang H, Wang J, Gordon R, et al. (2009) Atomic layer deposition of lanthanum-based ternary oxides. *Electrochem Solid-State Lett* 12: G13–G15.
136. Abdulagatov AI, Hall RA, Sutherland JL, et al. (2012) Molecular layer deposition of titanicone films using $TiCl_4$ and ethylene glycol or glycerol: growth and properties. *Chem Mater* 24: 2854–2863.
137. Kim H, Jeong G, Kim Y, et al. (2013) Metallic anodes for next generation secondary batteries. *Chem Soc Rev* 42: 9011–9034.
138. George SM, Lee BH, Yoon B, et al. (2011) Metalcones: Hybrid organic–inorganic films fabricated using atomic and molecular layer deposition techniques. *J Nanosci Nanotechno* 11: 7948–7955.

139. Marichy C, Bechelany M, Pinna N (2012) Atomic layer deposition of nanostructured materials for energy and environmental applications. *Adv Mater* 24: 1017–1032.
140. Hwang CS (2012) Atomic layer deposition for microelectronic applications, In: Pinna N, Knez M, *Atomic layer deposition of nanostructured materials*, John Wiley & Sons, 161–192.
141. Shao H, Umemoto S, Kikutani T, et al. (1997) Layer-by-layer polycondensation of nylon 66 by alternating vapour deposition polymerization. *Polymer* 38: 459–462.
142. Kim A, Filler MA, Kim S, et al. (2005) Layer-by-layer growth on Ge (100) via spontaneous urea coupling reactions. *J Am Chem Soc* 127: 6123–6132.
143. Lee JS, Lee YJ, Tae EL, et al. (2003) Synthesis of zeolite as ordered multicrystal arrays. *Science* 301: 818–821.
144. Haq S, Richardson N (1999) Organic beam epitaxy using controlled PMDA-ODA coupling reactions on Cu {110}. *J Phys Chem B* 103: 5256–5265.
145. Putkonen M, Harjuoja J, Sajavaara T, et al. (2007) Atomic layer deposition of polyimide thin films. *J Mater Chem* 17: 664–669.
146. Yoshimura T, Ito S, Nakayama T, et al. (2007) Orientation-controlled molecule-by-molecule polymer wire growth by the carrier-gas-type organic chemical vapor deposition and the molecular layer deposition. *Appl Phys Lett* 91: 033103.
147. Dameron AA, Seghete D, Burton B, et al. (2008) Molecular layer deposition of alucone polymer films using trimethylaluminum and ethylene glycol. *Chem Mater* 20: 3315–3326.
148. Yoon B, O'Patchen JL, Seghete D, et al. (2009) Molecular layer deposition of hybrid organic–inorganic polymer films using diethylzinc and ethylene glycol. *Chem Vapor Depos* 15: 112–121.
149. Peng Q, Gong B, VanGundy RM, et al. (2009) "Zincone" zinc oxide–organic hybrid polymer thin films formed by molecular layer deposition. *Chem Mater* 21: 820–830.
150. Yoon B, Lee Y, Derk A, et al. (2011) Molecular layer deposition of conductive hybrid organic–inorganic thin films using diethylzinc and hydroquinone. *ECS Trans* 33: 191–195.
151. Yoon B, Lee BH, George SM (2011) Molecular layer deposition of flexible, transparent and conductive hybrid organic–inorganic thin films. *ECS Trans* 41: 271–277.
152. Yoon B, Lee BH, George SM (2012) Highly conductive and transparent hybrid organic–inorganic zincone thin films using atomic and molecular layer deposition. *J Phys Chem C* 116: 24784–24791.
153. Han KS, Sung MM (2014) Molecular layer deposition of organic–inorganic hybrid films using diethylzinc and trihydroxybenzene. *J Nanosci Nanotechno* 14: 6137–6142.
154. Cho S, Han G, Kim K, et al. (2011) High-performance two-dimensional polydiacetylene with a hybrid inorganic–organic structure. *Angew Chem Int Edit* 50: 2742–2746.
155. Brown JJ, Hall RA, Kladitis PE, et al. (2013) Molecular layer deposition on carbon nanotubes. *ACS nano* 7: 7812–7823.
156. Lee BH, Anderson VR, George SM (2013) Molecular layer deposition of zircone and ZrO_2/zircone alloy films: growth and properties. *Chem Vapor Depos* 19: 204–212.
157. Hall RA, George SM, Kim Y, et al. (2014) Growth of zircone on nanoporous alumina using molecular layer deposition. *JOM* 66: 649–653.
158. Van de Kerckhove K, Mattelaer F, Deduytsche D, et al. (2016) Molecular layer deposition of "titanicone", a titanium-based hybrid material, as an electrode for lithium-ion batteries. *Dalton T* 45: 1176–1184.

159. Cao Y, Zhu L, Li X, et al. (2015) Growth characteristics of Ti-based fumaric acid hybrid thin films by molecular layer deposition. *Dalton T* 44: 14782–14792.
160. Chen C, Li P, Wang G, et al. (2013) Nanoporous nitrogen-doped titanium dioxide with excellent photocatalytic activity under visible light irradiation produced by molecular layer deposition. *Angew Chem Int Edit* 52: 9196–9200.
161. Lee BH, Anderson VR, George SM (2014) Growth and properties of hafnicone and HfO_2/hafnicone nanolaminate and alloy films using molecular layer deposition techniques. *ACS Appl Mater Inter* 6: 16880–16887.
162. Van de Kerckhove K, Mattelaer F, Dendooven J, et al. (2017) Molecular layer deposition of "vanadicone", a vanadium-based hybrid material, as an electrode for lithium-ion batteries. *Dalton T* 46: 4542–4553.
163. Meng X (2017) An overview of molecular layer deposition for organic and organic–inorganic hybrid materials: Mechanisms, growth characteristics, and promising applications. *J Mater Chem A* 5: 18326–18378.
164. Sveshnikova G, Kol'tsov S, Aleskovskii V (1967) Overview of early publications on atomic layer deposition. *J Appl Chem USSR* 40: 2644–2646.
165. Kol'tsov S, Sveshnikova G, Aleskovskii V (1969) Reaction of titanium tetrachloride with silicon. *Izv VUZ Khim Khim Tekhnol* 12: 562–564.
166. Suntola T (2014) From Ideas to global industry—40 years of ALD in Finland. *12th International Baltic ALD Conference*.
167. Yu M, Wang A, Wang Y, et al. (2014) An alumina stabilized ZnO-graphene anode for lithium ion batteries via atomic layer deposition. *Nanoscale* 6: 11419–11424.
168. Boukhalfa S, Evanoff K, Yushin G (2012) Atomic layer deposition of vanadium oxide on carbon nanotubes for high-power supercapacitor electrodes. *Energ Environ Sci* 5: 6872–6879.
169. Liu M, Li X, Karuturi SK, et al. (2012) Atomic layer deposition for nanofabrication and interface engineering. *Nanoscale* 4: 1522–1528.
170. Meng X, Yang X, Sun X (2012) Emerging applications of atomic layer deposition for lithium–ion battery studies. *Adv Mater* 24: 3589–3615.
171. Sun X, Xie M, Wang G, et al. (2012) Atomic layer deposition of TiO_2 on graphene for supercapacitors. *J Electrochem Soc* 159: A364–A369.
172. Meng X, Wang X, Geng D, et al. (2017) Atomic layer deposition for nanomaterial synthesis and functionalization in energy technology. *Mater Horiz* 4: 133–154.
173. Johansson A, Törndahl T, Ottosson L, et al. (2003) Copper nanoparticles deposited inside the pores of anodized aluminium oxide using atomic layer deposition. *Mat Sci Eng C-Mater* 23: 823–826.
174. Ferguson J, Buechler K, Weimer A, et al. (2005) SnO_2 atomic layer deposition on ZrO_2 and Al nanoparticles: Pathway to enhanced thermite materials. *Powder Technol* 156: 154–163.
175. Hakim LF, Portman JL, Casper MD, et al. (2004) Conformal coating of nanoparticles using atomic layer deposition in a fluidized bed reactor. *AIChE Annual Meeting, Conference Proceedings*, 6543–6563.
176. Hakim LF, Blackson J, George SM, et al. (2005) Nanocoating individual silica nanoparticles by atomic layer deposition in a fluidized bed reactor. *Chem Vapor Depos* 11: 420–425.
177. Hakim LF, George SM, Weimer AW (2005) Conformal nanocoating of zirconia nanoparticles by atomic layer deposition in a fluidized bed reactor. *Nanotechnology* 16: S375–S381.

178. Standridge SD, Schatz GC, Hupp JT (2009) Toward plasmonic solar cells: protection of silver nanoparticles via atomic layer deposition of TiO_2. *Langmuir* 25: 2596–2600.
179. Wank JR, George SM, Weimer AW (2004) Nanocoating individual cohesive boron nitride particles in a fluidized bed by ALD. *Powder Technol* 142: 59–69.
180. Wang G, Peng X, Yu L, et al. (2015) Enhanced microwave absorption of ZnO coated with Ni nanoparticles produced by atomic layer deposition. *J Mater Chem A* 3: 2734–2740.
181. Kei C, Cheng P, Liu D, et al. (2006) Smooth and conformal Al_2O_3 coating on polystyrene nanospheres by using atomic layer deposition. *J Vac Soc R.O.C.* 19: 48–51.
182. Ras RH, Kemell M, de Wit J, et al. (2007) Hollow inorganic nanospheres and nanotubes with tunable wall thicknesses by atomic layer deposition on self-assembled polymeric templates. *Adv Mater* 19: 102–106.
183. Justh N, Bakos LP, Hernádi K, et al. (2017) Photocatalytic hollow TiO_2 and ZnO nanospheres prepared by atomic layer deposition. *Sci Rep* 7: 4337.
184. Park HK, Yoon SW, Do YR (2013) Fabrication of wafer-scale TiO_2 nanobowl arrays via a scooping transfer of polystyrene nanospheres and atomic layer deposition for their application in photonic crystals. *J Mater Chem C* 1: 1732–1738.
185. Qin Y, Kim Y, Zhang L, et al. (2010) Preparation and elastic properties of helical nanotubes obtained by atomic layer deposition with carbon nanocoils as templates. *Small* 6: 910–914.
186. Weimer MA, Hakim LF, King DM, et al. (2008) Ultrafast metal-insulator varistors based on tunable Al_2O_3 tunnel junctions. *Appl Phys Lett* 92: 164101.
187. King DM, Liang X, Carney CS, et al. (2008) Atomic layer deposition of UV-absorbing ZnO films on SiO_2 and TiO_2 nanoparticles using a fluidized bed reactor. *Adv Funct Mater* 18: 607–615.
188. Hakim LF, King DM, Zhou Y, et al. (2007) Nanoparticle coating for advanced optical, mechanical and rheological properties. *Adv Funct Mater* 17: 3175–3181.
189. Wank JR, George SM, Weimer AW (2001) Vibro-fluidization of fine boron nitride powder at low pressure. *Powder Technol* 121: 195–204.
190. Solanki R, Huo J, Freeouf J, et al. (2002) Atomic layer deposition of ZnSe/CdSe superlattice nanowires. *Appl Phys Lett* 81: 3864–3866.
191. Min Y, Bae EJ, Jeong KS, et al. (2003) Ruthenium oxide nanotube arrays fabricated by atomic layer deposition using a carbon nanotube template. *Adv Mater* 15: 1019–1022.
192. Liu J, Meng X, Banis MN, et al. (2012) Crystallinity-controlled synthesis of zirconium oxide thin films on nitrogen-doped carbon nanotubes by atomic layer deposition. *J Phys Chem C* 116: 14656–14664.
193. Meng X, Liu J, Li X, et al. (2013) Atomic layer deposited $Li_4Ti_5O_{12}$ on nitrogen-doped carbon nanotubes. *RSC Adv* 3: 7285–7288.
194. Meng X, Zhong Y, Sun Y, et al. (2011) Nitrogen-doped carbon nanotubes coated by atomic layer deposited SnO_2 with controlled morphology and phase. *Carbon* 49: 1133–1144.
195. Meng X, Banis MN, Geng D, et al. (2013) Controllable atomic layer deposition of one-dimensional nanotubular TiO_2. *Appl Surf Sci* 266: 132–140.
196. Meng X, Riha SC, Libera JA, et al. (2015) Tunable core–shell single-walled carbon nanotube–Cu_2S networked nanocomposites as high-performance cathodes for lithium-ion batteries. *J Power Sources* 280: 621–629.

197. Meng X, He K, Su D, et al. (2014) Gallium sulfide–single-walled carbon nanotube composites: high-performance anodes for lithium-ion batteries. *Adv Funct Mater* 24: 5435–5442.
198. Meng X, Ionescu M, Banis MN, et al. (2011) Heterostructural coaxial nanotubes of CNT@Fe_2O_3 via atomic layer deposition: effects of surface functionalization and nitrogen-doping. *J Nanopart Res* 13: 1207–1218.
199. Elam JW, Xiong G, Han CY, et al. (2006) Atomic layer deposition for the conformal coating of nanoporous materials. *J Nanomater* 2006: 64501.
200. Meng X, Zhang Y, Sun S, et al. (2011) Three growth modes and mechanisms for highly structure-tunable SnO_2 nanotube arrays of template-directed atomic layer deposition. *J Mater Chem* 21: 12321–12330.
201. Hwang YJ, Hahn C, Liu B, et al. (2012) Photoelectrochemical properties of TiO_2 nanowire arrays: a study of the dependence on length and atomic layer deposition coating. *ACS Nano* 6: 5060–5069.
202. Göbelt M, Keding R, Schmitt SW, et al. (2015) Encapsulation of silver nanowire networks by atomic layer deposition for indium-free transparent electrodes. *Nano Energy* 16: 196–206.
203. Tak Y, Yong K (2005) ZrO_2-coated SiC nanowires prepared by plasma-enhanced atomic layer chemical vapor deposition. *Surf Rev Lett* 12: 215–219.
204. Gopireddy D, Takoudis CG, Gamota D, et al. (2005) Fabrication of silicon nanowires using atomic layer deposition. *2005 NSTI Nanotechnology Conference and Trade Show-NSTI Nanotech*, 2: 515–517.
205. Lu Y, Bangsaruntip S, Wang X, et al. (2006) DNA functionalization of carbon nanotubes for ultrathin atomic layer deposition of high κ dielectrics for nanotube transistors with 60 mV/decade switching. *J Am Chem Soc* 128: 3518–3519.
206. Bachmann J, Jing J, Knez M, et al. (2007) Ordered iron oxide nanotube arrays of controlled geometry and tunable magnetism by atomic layer deposition. *J Am Chem Soc* 129: 9554–9555.
207. Min Y, Bae EJ, Park JB, et al. (2007) ZnO nanoparticle growth on single-walled carbon nanotubes by atomic layer deposition and a consequent lifetime elongation of nanotube field emission. *Appl Phys Lett* 90: 263104.
208. Nakashima Y, Ohno Y, Kishimoto S, et al. (2010) Fabrication process of carbon nanotube field effect transistors using atomic layer deposition passivation for biosensors. *J Nanosci Nanotechno* 10: 3805–3809.
209. Kukli K, Ihanus J, Ritala M, et al. (1997) Properties of Ta_2O_5-based dielectric nanolaminates deposited by atomic layer epitaxy. *J Electrochem Soc* 144: 300–306.
210. Elam J, Sechrist Z, George S (2002) ZnO/Al_2O_3 nanolaminates fabricated by atomic layer deposition: growth and surface roughness measurements. *Thin Solid Films* 414: 43–55.
211. Zhang H, Solanki R (2001) Atomic layer deposition of high dielectric constant nanolaminates. *J Electrochem Soc* 148: F63–F66.
212. Ishii M, Iwai S, Kawata H, et al. (1997) Atomic layer epitaxy of AlP and its application to X-ray multilayer mirror. *J Cryst Growth* 180: 15–21.
213. Zhong L, Daniel WL, Zhang Z, et al. (2006) Atomic layer deposition, characterization, and dielectric properties of HfO_2/SiO_2 nanolaminates and comparisons with their homogeneous mixtures. *Chem Vapor Depos* 12: 143–150.

214. Ginestra CN, Sreenivasan R, Karthikeyan A, et al. (2007) Atomic layer deposition of Y_2O_3/ZrO_2 nanolaminates a route to ultrathin solid-state electrolyte membranes. *Electrochem Solid-State Lett* 10: B161–B165.
215. Zaitsu S, Jitsuno T, Nakatsuka M, et al. (2002) Optical thin films consisting of nanoscale laminated layers. *Appl Phys Lett* 80: 2442–2444.
216. Härkönen E, Díaz B, Światowska J, et al. (2011) Corrosion protection of steel with oxide nanolaminates grown by atomic layer deposition. *J Electrochem Soc* 158: C369–C378.
217. Graugnard E, King JS, Gaillot DP, et al. (2006) Sacrificial-layer atomic layer deposition for fabrication of non-close-packed inverse-opal photonic crystals. *Adv Funct Mater* 16: 1187–1196.
218. King J, Heineman D, Graugnard E, et al. (2005) Atomic layer deposition in porous structures: 3D photonic crystals. *Appl Surf Sci* 244: 511–516.
219. Kim E, Vaynzof Y, Sepe A, et al. (2014) Gyroid-structured 3D ZnO networks made by atomic layer deposition. *Adv Funct Mater* 24: 863–872.
220. Meng X, Geng D, Liu J, et al. (2010) Non-aqueous approach to synthesize amorphous/crystalline metal oxide–graphene nanosheet hybrid composites. *J Phys Chem C* 114: 18330–18337.
221. Liu J, Meng X, Hu Y, et al. (2013) Controlled synthesis of zirconium oxide on graphene nanosheets by atomic layer deposition and its growth mechanism. *Carbon* 52: 74–82.
222. Liang X, Yu M, Li J, et al. (2009) Ultra-thin microporous–mesoporous metal oxide films prepared by molecular layer deposition (MLD). *Chem Commun* 7140–7142.
223. Yang P, Wang G, Gao Z, et al. (2013) Uniform and conformal carbon nanofilms produced based on molecular layer deposition. *Materials* 6: 5602–5612.
224. Lee S, Baek G, Lee J, et al. (2018) Facile fabrication of p-type Al_2O_3/carbon nanocomposite films using molecular layer deposition. *Appl Surf Sci* 458: 864–871.
225. Liang X, Evanko BW, Izar A, et al. (2013) Ultrathin highly porous alumina films prepared by alucone ABC molecular layer deposition (MLD). *Micropor Mesopor Mat* 168: 178–182.
226. Liang X, King DM, Li P, et al. (2009) Nanocoating hybrid polymer films on large quantities of cohesive nanoparticles by molecular layer deposition. *AIChE J* 55: 1030–1039.
227. Abdulagatov AI, Terauds KE, Travis JJ, et al. (2013) Pyrolysis of titanicone molecular layer deposition films as precursors for conducting TiO_2/carbon composite films. *J Phys Chem C* 117: 17442–17450.
228. Qin L, Yan N, Hao H, et al. (2018) Surface engineering of zirconium particles by molecular layer deposition: Significantly enhanced electrostatic safety at minimum loss of the energy density. *Appl Surf Sci* 436: 548–555.
229. DuMont JW, George SM (2015) Pyrolysis of alucone molecular layer deposition films studied using in situ transmission Fourier transform infrared spectroscopy. *J Phys Chem C* 119: 14603–14612.
230. Luo L, Yang H, Yan P, et al. (2015) Surface-coating regulated lithiation kinetics and degradation in silicon nanowires for lithium ion battery. *ACS Nano* 9: 5559–5566.
231. Qin Y, Yang Y, Scholz R, et al. (2011) Unexpected oxidation behavior of Cu nanoparticles embedded in porous alumina films produced by molecular layer deposition. *Nano Lett* 11: 2503–2509.

232. Loebl AJ, Oldham CJ, Devine CK, et al. (2013) Solid electrolyte interphase on lithium-ion carbon nanofiber electrodes by atomic and molecular layer deposition. *J Electrochem Soc* 160: A1971–A1978.
233. Gong B, Peng Q, Parsons GN (2011) Conformal organic–inorganic hybrid network polymer thin films by molecular layer deposition using trimethylaluminum and glycidol. *J Phys Chem B* 115: 5930–5938.
234. Chen Y, Zhang B, Gao Z, et al. (2015) Functionalization of multiwalled carbon nanotubes with uniform polyurea coatings by molecular layer deposition. *Carbon* 82: 470–478.
235. Lushington A, Liu J, Bannis MN, et al. (2015) A novel approach in controlling the conductivity of thin films using molecular layer deposition. *Appl Surf Sci* 357: 1319–1324.
236. Nisula M, Karppinen M (2018) In situ lithiated quinone cathode for ALD/MLD-fabricated high-power thin-film battery. *J Mater Chem A* 6: 7027–7033.
237. Lee BH, Im KK, Lee KH, et al. (2009) Molecular layer deposition of ZrO_2-based organic–inorganic nanohybrid thin films for organic thin film transistors. *Thin Solid Films* 517: 4056–4060.
238. Lee BH, Ryu MK, Choi S, et al. (2007) Rapid vapor-phase fabrication of organic–inorganic hybrid superlattices with monolayer precision. *J Am Chem Soc* 129: 16034–16041.
239. Huang J, Lee M, Lucero A, et al. (2013) Organic–inorganic hybrid nano-laminates fabricated by ozone-assisted molecular–atomic layer deposition. *Chem Vapor Depos* 19: 142–148.
240. Tynell T, Yamauchi H, Karppinen M (2014) Hybrid inorganic–organic superlattice structures with atomic layer deposition/molecular layer deposition. *J Vac Sci Technol A* 32: 01A105.
241. Lee BH, Yoon B, Anderson VR, et al. (2012) Alucone alloys with tunable properties using alucone molecular layer deposition and Al_2O_3 atomic layer deposition. *J Phys Chem C* 116: 3250–3257.
242. Xiao W, Yu D, Bo SF, et al. (2014) The improvement of thin film barrier performances of organic–inorganic hybrid nanolaminates employing a low-temperature MLD/ALD method. *RSC Adv* 4: 43850–43856.
243. Loscutoff PW, Zhou H, Clendenning SB, et al. (2009) Formation of organic nanoscale laminates and blends by molecular layer deposition. *ACS Nano* 4: 331–341.
244. Yoon KH, Kim HS, Han KS, et al. (2017) Extremely high barrier performance of organic–inorganic nanolaminated thin films for organic light-emitting diodes. *ACS Appl Mater Inter* 9: 5399–5408.
245. Yoon K, Han K, Sung M (2012) Fabrication of a new type of organic–inorganic hybrid superlattice films combined with titanium oxide and polydiacetylene. *Nanoscale Res Lett* 7: 71.
246. Ahvenniemi E, Karppinen M (2016) Atomic/molecular layer deposition: a direct gas-phase route to crystalline metal–organic framework thin films. *Chem Commun* 52: 1139–1142.
247. Lausund KB, Petrovic V, Nilsen O (2017) All-gas-phase synthesis of amino-functionalized UiO-66 thin films. *Dalton T* 46: 16983–16992.
248. Lemaire PC, Zhao J, Williams PS, et al. (2016) Copper benzenetricarboxylate metal–organic framework nucleation mechanisms on metal oxide powders and thin films formed by atomic layer deposition. *ACS Appl Mater Inter* 8: 9514–9522.
249. Stassen I, De Vos D, Ameloot R (2016) Vapor-phase deposition and modification of metal–organic frameworks: State-of-the-art and future directions. *Chem-Eur J* 22: 14452–14460.

250. Ahvenniemi E, Karppinen M (2016) In situ atomic/molecular layer-by-layer deposition of inorganic–organic coordination network thin films from gaseous precursors. *Chem Mater* 28: 6260–6265.
251. Salmi LD, Heikkilä MJ, Vehkamäki M, et al. (2015) Studies on atomic layer deposition of IRMOF-8 thin films. *J Vac Sci Technol A* 33: 01A121.
252. Salmi LD, Heikkilä MJ, Puukilainen E, et al. (2013) Studies on atomic layer deposition of MOF-5 thin films. *Micropor Mesopor Mat* 182: 147–154.
253. Herrera JE, Kwak JH, Hu JZ, et al. (2006) Synthesis of nanodispersed oxides of vanadium, titanium, molybdenum, and tungsten on mesoporous silica using atomic layer deposition. *Top Catal* 39: 245–255.
254. Kemell M, Pore V, Tupala J, et al. (2007) Atomic layer deposition of nanostructured TiO_2 photocatalysts via template approach. *Chem Mater* 19: 1816–1820.
255. Sander MS, Côté MJ, Gu W, et al. (2004) Template-assisted fabrication of dense, aligned arrays of titania nanotubes with well-controlled dimensions on substrates. *Adv Mater* 16: 2052–2057.
256. Biercuk M, Monsma D, Marcus C, et al. (2003) Low-temperature atomic-layer-deposition lift-off method for microelectronic and nanoelectronic applications. *Appl Phys Lett* 83: 2405–2407.
257. Seo EK, Lee JW, Sung-Suh HM, et al. (2004) Atomic layer deposition of titanium oxide on self-assembled-monolayer-coated gold. *Chem Mater* 16: 1878–1883.
258. Wang XD, Graugnard E, King JS, et al. (2004) Large-scale fabrication of ordered nanobowl arrays. *Nano Lett* 4: 2223–2226.
259. Romanes MC (2008) Structure and low-temperature tribology of lubricious nanocrystalline zinc oxide/aluminium oxide nanolaminates and zirconium dioxide monofilms grown by atomic layer deposition [PhD thesis]. University of North Texas.
260. Miikkulainen V, Leskelä M, Ritala M, et al. (2013) Crystallinity of inorganic films grown by atomic layer deposition: Overview and general trends. *J Appl Phys* 113: 2.
261. Sechrist Z, Schwartz B, Lee J, et al. (2006) Modification of opal photonic crystals using Al_2O_3 atomic layer deposition. *Chem Mater* 18: 3562–3570.
262. Halbur JC, Padbury RP, Jur JS (2013) Induced wetting of polytetrafluoroethylene by atomic layer deposition for application of aqueous-based nanoparticle inks. *Mater Lett* 101: 25–28.
263. Dafinone MI, Feng G, Brugarolas T, et al. (2011) Mechanical reinforcement of nanoparticle thin films using atomic layer deposition. *ACS Nano* 5: 5078–5087.
264. Gong B, Spagnola JC, Parsons GN (2012) Hydrophilic mechanical buffer layers and stable hydrophilic finishes on polydimethylsiloxane using combined sequential vapor infiltration and atomic/molecular layer deposition. *J Vac Sci Technol A* 30: 01A156.
265. Doll G, Mensah B, Mohseni H, et al. (2010) Chemical vapor deposition and atomic layer deposition of coatings for mechanical applications. *J Therm Spray Techn* 19: 510–516.
266. Miller DC, Foster RR, Zhang Y, et al. (2009) The mechanical robustness of atomic-layer-and molecular-layer-deposited coatings on polymer substrates. *J Appl Phys* 105: 093527.
267. Miller DC, Foster RR, Jen S, et al. (2009) Thermomechanical properties of aluminum alkoxide (alucone) films created using molecular layer deposition. *Acta Mater* 57: 5083–5092.
268. Sun S, Zhang G, Gauquelin N, et al. (2013) Single-atom catalysis using Pt/graphene achieved through atomic layer deposition. *Sci Rep* 3: 1775.
269. Christensen ST, Feng H, Libera JL, et al. (2010) Supported Ru–Pt bimetallic nanoparticle catalysts prepared by atomic layer deposition. *Nano Lett* 10: 3047–3051.

270. Ishchuk S, Taffa DH, Hazut O, et al. (2012) Transformation of organic–inorganic hybrid films obtained by molecular layer deposition to photocatalytic layers with enhanced activity. *ACS Nano* 6: 7263–7269.
271. Sarkar D, Ishchuk S, Taffa DH, et al. (2016) Oxygen-deficient titania with adjustable band positions and defects; molecular layer deposition of hybrid organic–inorganic thin films as precursors for enhanced photocatalysis. *J Phys Chem C* 120: 3853–3862.
272. Argyle MD, Bartholomew CH (2015) Heterogeneous catalyst deactivation and regeneration: a review. *Catalysts* 5: 145–269.
273. O'Neill BJ, Jackson DH, Crisci AJ, et al. (2013) Stabilization of copper catalysts for liquid-phase reactions by atomic layer deposition. *Angew Chem* 125: 14053–14057.
274. Feng H, Lu J, Stair PC, et al. (2011) Alumina over-coating on Pd nanoparticle catalysts by atomic layer deposition: Enhanced stability and reactivity. *Catal Lett* 141: 512–517.
275. Liang X, Li J, Yu M, et al. (2011) Stabilization of supported metal nanoparticles using an ultrathin porous shell. *ACS Catal* 1: 1162–1165.
276. Gould TD, Izar A, Weimer AW, et al. (2014) Stabilizing Ni catalysts by molecular layer deposition for harsh, dry reforming conditions. *ACS Catal* 4: 2714–2717.
277. Zhang B, Chen Y, Li J, et al. (2015) High efficiency Cu–ZnO hydrogenation catalyst: the tailoring of Cu–ZnO interface sites by molecular layer deposition. *ACS Catal* 5: 5567–5573.
278. Avni A, Blázquez MA (2011) Can plant biotechnology help in solving our food and energy shortage in the future? *Curr Opin Biotech* 22: 220–223.
279. Papon P (2008) Énergie: science et technique, remparts contre la pénurie? *Futuribles* 346: 39–54.
280. Armaroli N, Balzani V (2007) The future of energy supply: challenges and opportunities. *Angew Chem Int Edit* 46: 52–66.
281. Cook TR, Dogutan DK, Reece SY, et al. (2010) Solar energy supply and storage for the legacy and nonlegacy worlds. *Chem Rev* 110: 6474–6502.
282. Nicoletti G, Arcuri N, Nicoletti G, et al. (2015) A technical and environmental comparison between hydrogen and some fossil fuels. *Energ Convers Manage* 89: 205–213.
283. Petrakopoulou F, Iribarren D, Dufour J (2015) Life-cycle performance of natural gas power plants with pre-combustion CO_2 capture. *Greenh Gases* 5: 268–276.
284. Modahl IS, Askham C, Lyng K, et al. (2012) Weighting of environmental trade-offs in CCS—an LCA case study of electricity from a fossil gas power plant with post-combustion CO_2 capture, transport and storage. *Int J Life Cycle Ass* 17: 932–943.
285. Korner C, Basler D (2010) Phenology under global warming. *Science* 327: 1461–1462.
286. Koven CD, Ringeval B, Friedlingstein P, et al. (2011) Permafrost carbon-climate feedbacks accelerate global warming. *P Natl Acad Sci USA* 108: 14769–14774.
287. Cox PM, Betts RA, Jones CD, et al. (2000) Acceleration of global warming due to carbon-cycle feedbacks in a coupled climate model. *Nature* 408: 184–187.
288. Root TL, Price JT, Hall KR, et al. (2003) Fingerprints of global warming on wild animals and plants. *Nature* 421: 57–60.
289. Yoshimura T, Tatsuura S, Sotoyama W (1991) Polymer films formed with monolayer growth steps by molecular layer deposition. *Appl Phys Lett* 59: 482–484.

290. Adamczyk N, Dameron A, George S (2008) Molecular layer deposition of poly(p-phenylene terephthalamide) films using terephthaloyl chloride and p-phenylenediamine. *Langmuir* 24: 2081–2089.
291. Du Y, George S (2007) Molecular layer deposition of nylon 66 films examined using in situ FTIR spectroscopy. *J Phys Chem C* 111: 8509–8517.
292. Loscutoff PW, Lee H, Bent SF (2010) Deposition of ultrathin polythiourea films by molecular layer deposition. *Chem Mater* 22: 5563–5569.
293. Yoshimura T, Tatsuura S, Sotoyama W, et al. (1992) Quantum wire and dot formation by chemical vapor deposition and molecular layer deposition of one-dimensional conjugated polymer. *Appl Phys Lett* 60: 268–270.
294. Ivanova TV, Maydannik PS, Cameron DC (2012) Molecular layer deposition of polyethylene terephthalate thin films. *J Vac Sci Technol A* 30: 01A121.
295. Meng X, Comstock DJ, Fister TT, et al. (2014) Vapor-phase atomic-controllable growth of amorphous Li_2S for high-performance lithium–sulfur batteries. *ACS Nano* 8: 10963–10972.
296. Cao Y, Meng X, Elam JW (2016) Atomic layer deposition of Li_xAl_yS solid-state electrolytes for stabilizing lithium–metal anodes. *ChemElectroChem* 3: 858–863.
297. Yan B, Li X, Bai Z, et al. (2017) A review of atomic layer deposition providing high performance lithium sulfur batteries. *J Power Sources* 338: 34–48.
298. Lei Y, Lu J, Luo X, et al. (2013) Synthesis of porous carbon supported palladium nanoparticle catalysts by atomic layer deposition: application for rechargeable lithium–O_2 battery. *Nano Lett* 13: 4182–4189.
299. Jung YS, Cavanagh AS, Dillon AC, et al. (2010) Enhanced stability of $LiCoO_2$ cathodes in lithium-ion batteries using surface modification by atomic layer deposition. *J Electrochem Soc* 157: A75–A81.
300. Jung YS, Cavanagh AS, Yan Y, et al. (2011) Effects of atomic layer deposition of Al_2O_3 on the $Li[Li_{0.20}Mn_{0.54}Ni_{0.13}Co_{0.13}]O_2$ cathode for lithium-ion batteries. *J Electrochem Soc* 158: A1298–A1302.
301. Zhao J, Wang Y (2013) Atomic layer deposition of epitaxial ZrO_2 coating on $LiMn_2O_4$ nanoparticles for high-rate lithium ion batteries at elevated temperature. *Nano Energy* 2: 882–889.
302. Chen H, Lin Q, Xu Q, et al. (2014) Plasma activation and atomic layer deposition of TiO_2 on polypropylene membranes for improved performances of lithium-ion batteries. *J Membrane Sci* 458: 217–224.
303. Xie M, Sun X, George SM, et al. (2015) Amorphous ultrathin SnO_2 films by atomic layer deposition on graphene network as highly stable anodes for lithium-ion batteries. *ACS Appl Mater Inter* 7: 27735–27742.
304. Fang X, Ge M, Rong J, et al. (2014) Ultrathin surface modification by atomic layer deposition on high voltage cathode $LiNi_{0.5}Mn_{1.5}O_4$ for lithium ion batteries. *Energy Technol* 2: 159–165.
305. Li Y, Sun Y, Xu G, et al. (2014) Tuning electrochemical performance of Si-based anodes for lithium-ion batteries by employing atomic layer deposition alumina coating. *J Mater Chem A* 2: 11417–11425.
306. Xie M, Sun X, Sun H, et al. (2016) Stabilizing an amorphous V_2O_5/carbon nanotube paper electrode with conformal TiO_2 coating by atomic layer deposition for lithium ion batteries. *J Mater Chem A* 4: 537–544.

307. Zhu B, Liu N, McDowell M, et al. (2015) Interfacial stabilizing effect of ZnO on Si anodes for lithium ion battery. *Nano Energy* 13: 620–625.
308. Piper DM, Travis JJ, Young M, et al. (2014) Reversible high-capacity Si nanocomposite anodes for lithium–ion batteries enabled by molecular layer deposition. *Adv Mater* 26: 1596–1601.
309. Chen L, Huang Z, Shahbazian-Yassar R, et al. (2018) Directly formed alucone on lithium metal for high-performance Li batteries and Li–S batteries with high sulfur mass loading. *ACS Appl Mater Inter* 10: 7043–7051.
310. Li X, Lushington A, Liu J, et al. (2014) Superior stable sulfur cathodes of Li–S batteries enabled by molecular layer deposition. *Chem Commun* 50: 9757–9760.
311. Liu J, Xiao B, Banis MN, et al. (2015) Atomic layer deposition of amorphous iron phosphates on carbon nanotubes as cathode materials for lithium-ion batteries. *Electrochim Acta* 162: 275–281.
312. Lu S, Wang H, Zhou J, et al. (2017) Atomic layer deposition of ZnO on carbon black as nanostructured anode materials for high-performance lithium-ion batteries. *Nanoscale* 9: 1184–1192.
313. Lee M, Su C, Lin Y, et al. (2013) Atomic layer deposition of TiO_2 on negative electrode for lithium ion batteries. *J Power Sources* 244: 410–416.
314. Nisula M, Karppinen M (2016) Atomic/molecular layer deposition of lithium terephthalate thin films as high rate capability Li-ion battery anodes. *Nano Lett* 16: 1276–1281.
315. Kim HG, Lee H (2017) Atomic layer deposition on 2D materials. *Chem Mater* 29: 3809–3826.
316. Mondloch JE, Bury W, Fairen-Jimenez D, et al. (2013) Vapor-phase metalation by atomic layer deposition in a metal-organic framework. *J Am Chem Soc* 135: 10294–10297.

AIMS Press

© 2018 the Author(s), licensee AIMS Press. This is an open access article distributed under the terms of the Creative Commons Attribution License (http://creativecommons.org/licenses/by/4.0)